

# 1 A model for cortical activity sequences

2 Andrew B. Lehr<sup>1,2,✉</sup>, Finn Erzmann<sup>1,2</sup>, Carlo Michaelis<sup>1,2</sup>, Julia Nowak<sup>3</sup>,  
3 Alexander Gail<sup>3</sup>, Arvind Kumar<sup>4</sup>, and Christian Tetzlaff<sup>1,2</sup>

4 <sup>1</sup>Department of Computational Neuroscience, University of Göttingen, Germany

5 <sup>2</sup>Group of Computational Synaptic Physiology, Department of Neuro- and Sensory Physiology,  
6 University Medical Center Göttingen, Germany

7 <sup>3</sup>Sensorimotor Group, German Primate Center, Göttingen, Germany

8 <sup>4</sup>Department of Computational Science and Technology, KTH Royal Institute of Technology, Sweden

9 <sup>✉</sup>Correspondence: andrew.lehr@med.uni-goettingen.de

## 10 Abstract

11 Networks of neurons in the brain, that act on a timescale of milliseconds, can  
12 intrinsically generate reliable sequential activity on slow behavioral timescales  
13 of seconds. A possible mechanism for intrinsic sequence generation based  
14 on theoretical evidence points to distance-dependent connectivity with cor-  
15 related spatial asymmetries, establishing an anisotropic network connectivity.  
16 We show that networks with such correlated asymmetric connectivity as well as  
17 symmetric distance-dependent connectivity match experimental data of con-  
18 nectivity motifs as well as neuronal activity statistics from rat and monkey  
19 cortex. At the network level, however, only the correlated asymmetric con-  
20 nectivity pattern generates spatiotemporal activity sequences on behaviorally  
21 relevant timescales, while the symmetric connectivity results in transient but  
22 stationary spatial bumps of neural activity. Our results strongly support the  
23 role of correlated asymmetries in connectivity for the generation of sequential  
24 activity in neural networks.

## 25 1 Introduction

26 Spatiotemporal sequences of neuronal activation have emerged as a key feature of network dy-  
27 namics in the brain. Sequential activity has been observed across brain regions and animal  
28 species in various behavioral tasks such as decision making<sup>1,2</sup>, timing<sup>3,4</sup>, olfactory processing<sup>5</sup>,  
29 birdsong generation<sup>6</sup>, motor control<sup>7–9</sup>, and hippocampal-dependent learning and memory<sup>10–19</sup>.  
30 Reproducible sequential activity can span hundreds of milliseconds up to minutes<sup>20</sup>, orders of  
31 magnitude longer than the timescale of single spikes. Crucially, sequences arise even without  
32 sequential input<sup>1,2,6,11,17,21</sup> suggesting that they can be intrinsically generated by the local net-  
33 work structure. However, the theoretical basis of how recurrently and locally connected spiking  
34 neurons can generate such sequences is a longstanding matter of active investigation<sup>22–41</sup>.

35 Experimental observations have revealed features of cortical connectivity thought to support  
36 intrinsic spatiotemporal sequence generation. The probability of a connection between neurons  
37 is distance-dependent, decreasing on a scale of hundreds of micrometers<sup>42–46</sup>. Therefore, a neu-  
38 ron has a higher probability to connect to its close neighbours. Neurons can furthermore have  
39 asymmetric projection patterns with axons or dendrites extending preferentially in a particular  
40 direction<sup>43–48</sup>. In mouse visual cortex, pyramidal neurons receive spatially asymmetric inputs  
41 that determine directional tuning<sup>46,49</sup>, with nearby neurons that were born together sharing  
42 inputs<sup>50</sup>. In mouse sensory cortex nearby neurons project preferentially in similar directions  
43 aligned with the propagation direction of travelling waves<sup>51</sup>, spatiotemporal sequences of neu-  
44 ronal activation that have been observed in many settings<sup>52–71</sup>.

45 From locally connected recurrent network models (LCRN), it is well known that symmetric  
46 distance-dependent connectivity supports the formation of spatially localized neuronal activity,  
47 referred to as “bumps”<sup>22,28,31,36,37,72,73</sup>. Furthermore, Spreizer et al.<sup>37</sup> show that a rather small,  
48 but correlated asymmetry in the distance-dependent connectivity can induce a movement of  
49 the localized bumps through the network resulting in spatiotemporal sequences on a timescale  
50 of several seconds. Based on these results, here, we perform a more detailed comparison to  
51 microcircuit connectivity data and neuronal firing statistics to demonstrate that correlated  
52 asymmetric connectivity provides a biologically reasonable model underlying the generation of  
53 neural spatiotemporal sequences.

54 On the microcircuits level, connections between neurons are not random but instead show en-  
55 hanced connectivity motifs like reciprocal connections, chains, convergence and divergence<sup>42,45,74–77</sup>.  
56 We show that locally connected networks reproduce the nonrandom connectivity motifs observed  
57 in cortex<sup>74</sup> regardless of whether projections are symmetric or correlated asymmetric. Further,  
58 by introducing heterogeneity in neuronal timescales<sup>78</sup> via a distribution of refractory periods<sup>79</sup>,

59 we show that neuronal activity resulting from both symmetric and correlated asymmetric connectivity can reliably match monkey motor/premotor cortex neuronal firing statistics. Thus,  
60 both types of connectivity, symmetric and correlated asymmetric, are consistent with cortical  
61 connectivity motifs as well as single neuron activity statistics of the cortex. At the network level,  
62 however, only correlated asymmetric connectivity generates spatiotemporal activity sequences  
63 on timescales of seconds.  
64

## 65 2 Results

### 66 2.1 Both symmetric and asymmetric distance-dependent projections 67 match cortical connectivity motifs

68 We first compared recurrent networks with distance-dependent connectivity to experimentally  
69 observed connectivity motifs from rat visual cortex<sup>74</sup>. We considered an *isotropic* model with  
70 symmetric distance-dependent connectivity in which a Gaussian kernel centered at each neu-  
71 ron defines the probability of forming a synapse with surrounding neurons. Furthermore, we  
72 considered an *anisotropic* model in which the center of the Gaussian kernel is slightly shifted  
73 introducing on average an asymmetry in the connectivity. For nearby neurons the shift and thus  
74 the asymmetry is correlated (Fig. 1a). Note that the level of asymmetry is small compared  
75 to the isotropic network (Fig. 1c), but sufficient to generate local bumps of increased activity  
76 moving through the network to form a spatiotemporal sequence (Fig. 1d). We varied two pa-  
77 rameters in both models (Fig. 2b): (i) the connection locality, i.e. standard deviation  $\sigma_{\text{loc,exc}}$   
78 of the Gaussian kernel for excitatory neurons, with a lower standard deviation implying more  
79 local connections, and (ii) the proportion of synapses formed randomly  $p_{\text{con,rand}}$ , independent of  
80 the Gaussian kernel. Connection locality  $\sigma_{\text{loc,exc}}$  ranged from 0.01 to 0.25 in steps of 0.01 and  
81 the proportion of random connections  $p_{\text{con,rand}}$  ranged from no random connections to 25% of  
82 the overall synapses chosen randomly in steps of 1%.

83 **Two-neuron motifs.** For pairs of neurons there are three possible motifs: bidirectional,  
84 unidirectional or no connection (Fig. 2a). In rat visual cortex data, Song et al.<sup>74</sup> observed  
85 that unidirectional connections are underrepresented while bidirectional connections are highly  
86 overrepresented compared to what is expected in a randomly connected network. We found that  
87 this result can be accurately reproduced by both the *isotropic* and *anisotropic* models (Fig. 2c  
88 and 2d, respectively). In both cases, a large region of the parameter space fit the data well  
89 (purple region and white contours, Fig. 2c,d). Both models fit the cortical motif data best  
90 for connection locality around  $\sigma_{\text{loc,exc}} = 0.14$  and with very low or no probability of random  
91 connections  $p_{\text{con,rand}} \approx 0$  (see Fig. 2c,d). Note that correlated asymmetry in the projections had

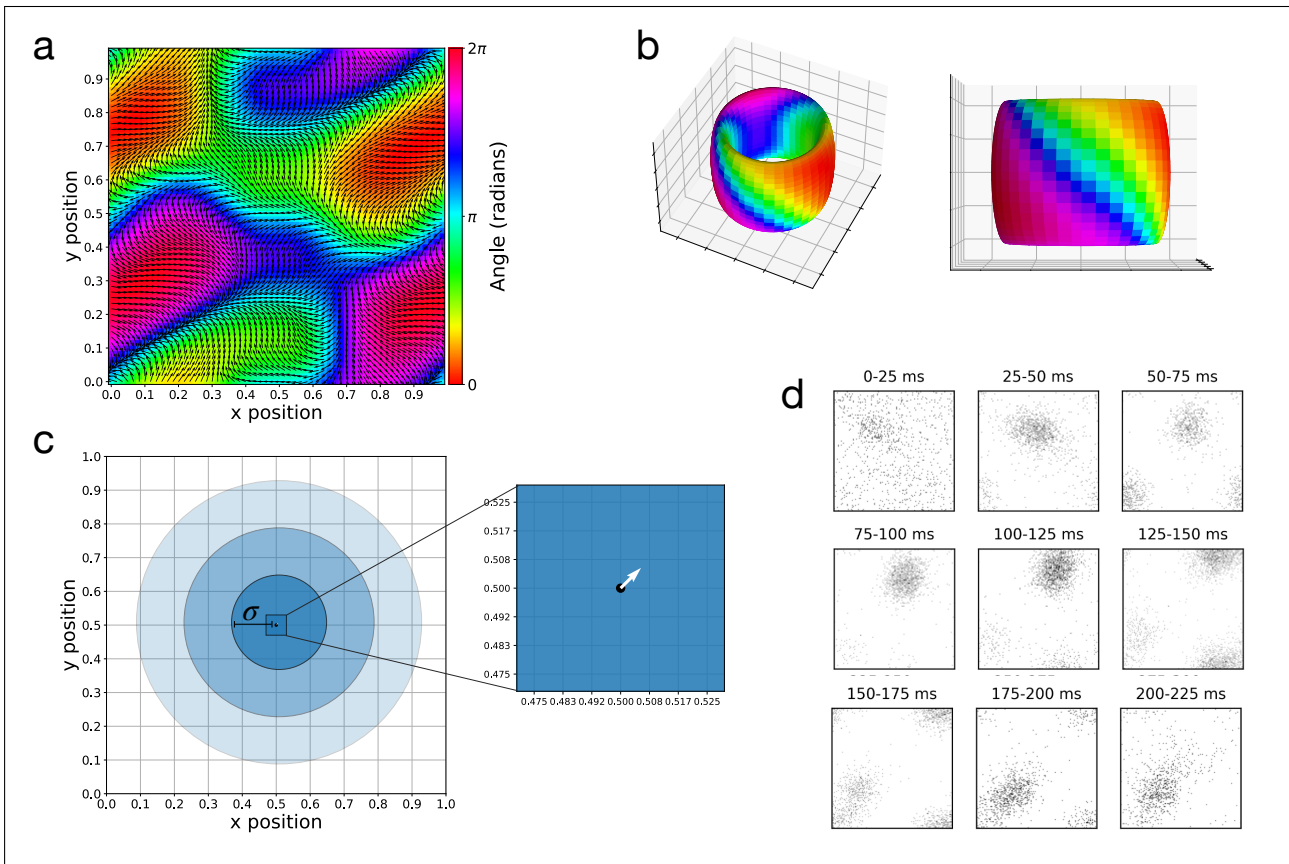


**Figure 1. The anisotropic network model.** (a) The Perlin connectivity landscape with preferred directions (angles) color coded and shown as a vector field. (b) The network has periodic boundary conditions and is thus folded to give a toroidal network topology. (c) An example Gaussian connectivity kernel with standard deviation  $\sigma = 0.14$  and shift  $d = 1$  is shown. Each ring is one standard deviation. Neurons are equidistantly spaced on the grid such that for a network with  $N = 14400$  excitatory neurons, one of the grid squares ( $0.1 \times 0.1$ ) contains 144 excitatory neurons. The zoom shows how small the shift is in comparison to the network size. In the zoomed region, one excitatory neuron is located at each grid corner. (d) Under these circumstances, spatially localized activity emerges in the network and given the correlated asymmetry, becomes “unstuck in space”, moving around the network. Each frame shows all spikes from a 25 ms time window in response to a transient spatially local burst of input arriving at 10 ms. A black dot was plotted for each spike at the location the corresponding neuron.

no observable effect on the motifs evidenced by the similarity of the *isotropic* and *anisotropic* results. The fit deteriorates when the proportion of random connections is increased (Fig. 2e,f), which is to be expected since for a randomly connected network with  $p_{\text{con},\text{rand}} = 1$ , all over- and underrepresentations should vanish, given that the measure is relative to motif counts in a random network.

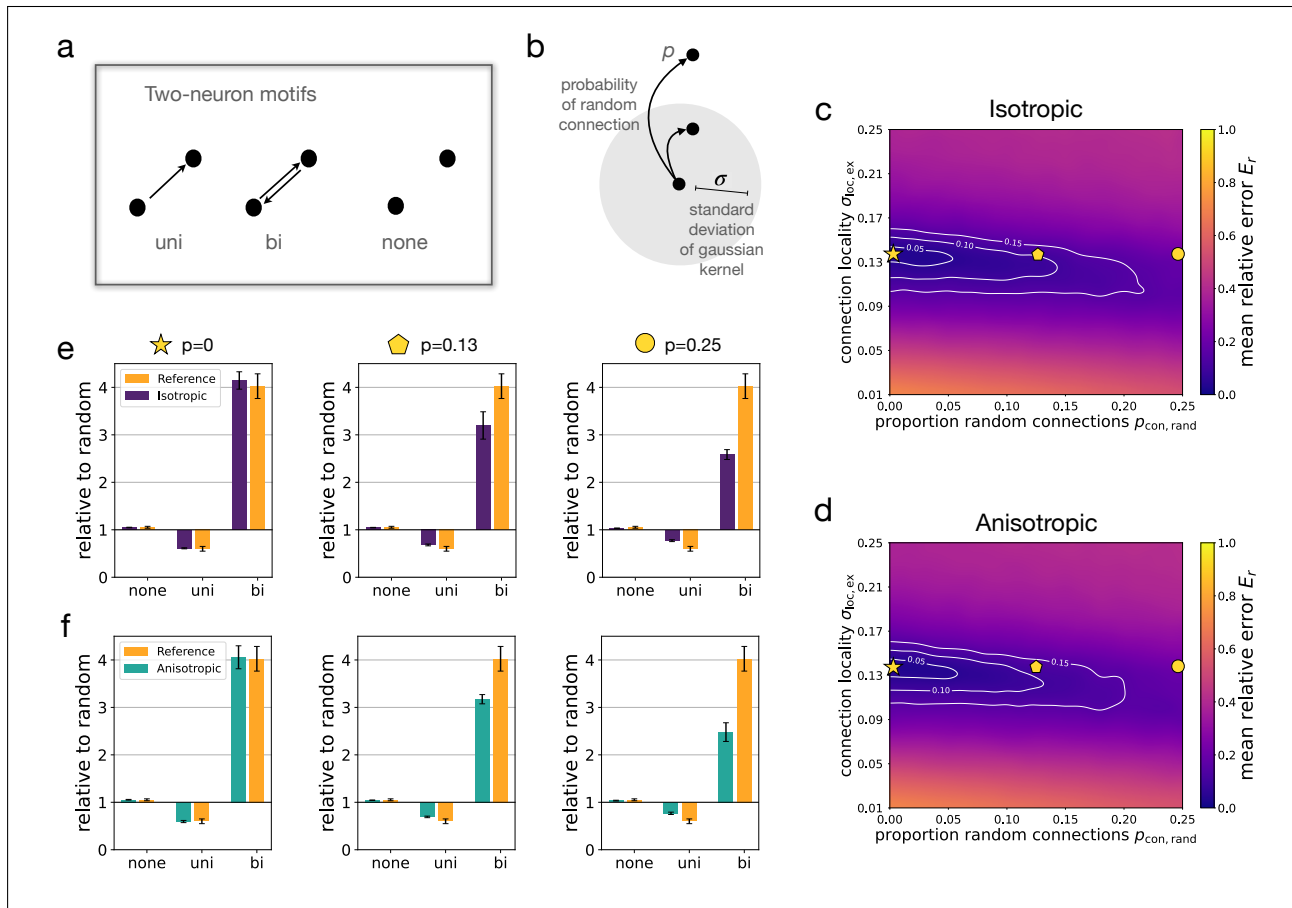


**Figure 2. Locally connected networks fit experimentally observed two-neuron connectivity motifs.** (a) The three possible two-neuron motifs are shown — unidirectional, bidirectional, or not connected. (b) Depiction of connectivity parameters that were varied. The standard deviation of the Gaussian connectivity kernel is parameterized by  $\sigma_{loc,exc}$  and the probability of a synapse being a random connection not defined by the Gaussian kernel is  $p_{con,rand}$  (shortened to  $\sigma$  and  $p$  in figure). (c) Mean relative error between two neuron connectivity motifs measured in the isotropic network model vs. rat visual cortex data<sup>74</sup>. (d) Same as (c) but for the anisotropic network model. Both (c) and (d) are averaged over 5 randomly generated networks drawn according to the parameters  $\sigma_{loc,exc}$  and  $p_{con,rand}$ . Graphs are smoothed and contours are added to aid visualization (see Methods). Shapes indicate parameter sets shown in (e,f). (e) Two-neuron connectivity motifs relative to expectation based on random connectivity is shown for the isotropic model (purple) for three examples each with  $\sigma_{loc,exc} = 0.14$  and increasing random connectivity  $p_{con,rand} = 0$ ,  $p_{con,rand} = 0.13$ , and  $p_{con,rand} = 0.25$ , compared to experimental data<sup>74</sup> (yellow). (f) Same as (e) but for the anisotropic network model (teal). Bars show mean  $\pm$  standard deviation over  $N_{seed} = 5$ .

97 **Three-neuron motifs.** For groups of three neurons, we again estimated the mean relative  
 98 error  $E_r$  for the same parameter space as for the two-neuron motifs ( $\sigma_{loc,exc} \in [0.01, 0.25]$  and  
 99  $p_{con,rand} \in [0, 0.25]$ ) in both models. The underlying connection probabilities  $p_{uni}$ ,  $p_{bi}$  and  $p_{none}$ ,

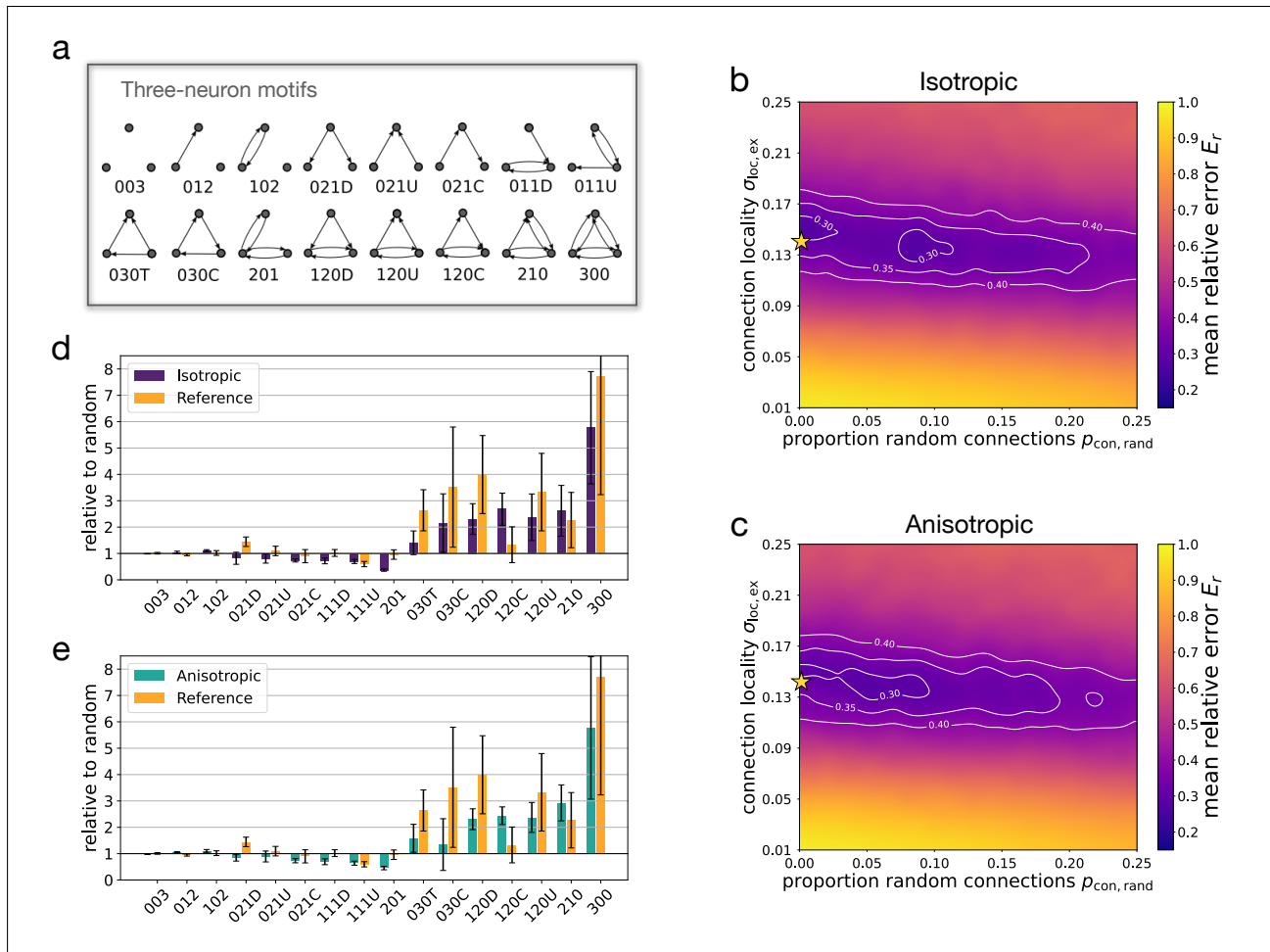


**Figure 3. Locally connected networks fit experimentally observed three-neuron connectivity motifs.** (a) The sixteen possible three-neuron motifs are shown. (b) Mean relative error between three-neuron connectivity motifs measured in the isotropic network model vs. rat visual cortex data<sup>74</sup>. (c) Same as (b) but for the anisotropic network model. Both (b) and (c) are averaged over 5 randomly generated networks drawn according to the parameters  $\sigma_{loc,exc}$  and  $p_{con,rand}$ . Graphs are smoothed and contours are added to aid visualization (see Methods). Stars indicate parameters used for examples shown in (d,e). (d) Three-neuron connectivity motifs relative to expectation based on observed two-neuron motifs (see Methods and Song et al.<sup>74</sup>) are shown for the isotropic model (purple) for parameters identified in two-neuron motif comparison above (gold star in (b),  $\sigma_{loc,exc} = 0.14$ ,  $p_{con,rand} = 0$ ) with comparison to experimental data<sup>74</sup> (yellow). (e) Same as (d) but for the anisotropic network model (teal). Bars show mean  $\pm$  standard deviation over  $N_{seed} = 5$ .

100 which are used to calculate the expected number of three-neuron motifs in a randomly connected  
 101 network (see Methods Section 4.8 and Table 2), are chosen based on the experimental results  
 102 for the two-neuron motifs from Song et al.<sup>74</sup>. For three-neuron motifs the region with the  
 103 lowest error has a similar position within the parameter space to the results for two-neuron

104 motifs, with anisotropic and isotropic model performing similarly (Fig. 3c,d). The values of  
105  $E_r$  are however larger for three-neuron motifs indicating a less accurate match compared to  
106 the two-neuron motifs, though this is compensated by larger standard deviations of observed  
107 three-neuron motifs in the experimental data and simulation (Fig. 3e,f). Fig. 3e,f shows over-  
108 and underrepresentations of the 16 different three-neuron motifs averaged over five network  
109 initializations for each model and the experimental data for comparison. The examples are  
110 taken from the region in the parameter space with lowest error for the two-neuron motifs (purple  
111 region in Fig. 2c,d,  $\sigma_{\text{loc},\text{exc}} = 0.14$ ,  $p_{\text{con},\text{rand}} = 0$ ). Two- and three-neuron motif counts for the  
112 best fits on triads and pairs are shown in Supplementary Fig. S1.

## 113 2.2 Neurons with distance-dependent projections and heterogeneous 114 refractory periods match single neuron cortical activity statis- 115 tics

116 With both the *isotropic* and *anisotropic* models being able to reproduce cortical microcircuit  
117 connectivity motifs, we next turned to neuronal activity statistics. We compared the models  
118 with experimental data from macaque monkey motor (M1) and premotor cortex (PMd) during  
119 a memory-guided center-out reach task in terms of firing rate distributions, interspike interval  
120 distributions, and the coefficient of variation (see Methods). For the simulations, connectivity  
121 in the models was based on the results of fitting the connectivity motifs,  $\sigma_{\text{loc},\text{exc}} = 0.14$  and  
122  $p_{\text{con},\text{rand}} = 0$ .

123 Since we were interested in intrinsically generated activity, we administered instantaneous spa-  
124 tially local bursts of input during ongoing background input. In order to fit the models to the  
125 activity statistics of experimental data, we introduced heterogeneity in neuronal timescales by  
126 considering a distribution of refractory periods  $\tau_{\text{ref}}$ , parameterized by the average refractory  
127 period  $\mu_\tau$  and the standard deviation of the refractory period distribution  $\sigma_\tau$  (Fig. 4a). For  
128 each refractory period distribution ( $\mu_\tau$ ,  $\sigma_\tau$ ) we ran five simulations of 500 milliseconds (based  
129 on average task duration in experimental data, see *Methods: Electrophysiological data*) for the  
130 *isotropic* and *anisotropic* networks, in which the recurrent connections and background input  
131 differed and the spatially local burst of input remained the same.

132 Both models were able to reproduce the activity statistics and the results were consistent over a  
133 range of refractory period distributions. Fig. 4e,f depict the difference between the models and  
134 experimental data when comparing the interspike interval distributions. The pattern of results  
135 demonstrate that heterogeneity is required to match the experimental data (purple region, white  
136 contours). When heterogeneity was low ( $\sigma_{\text{ref}}$  small), the models and experimental data were not

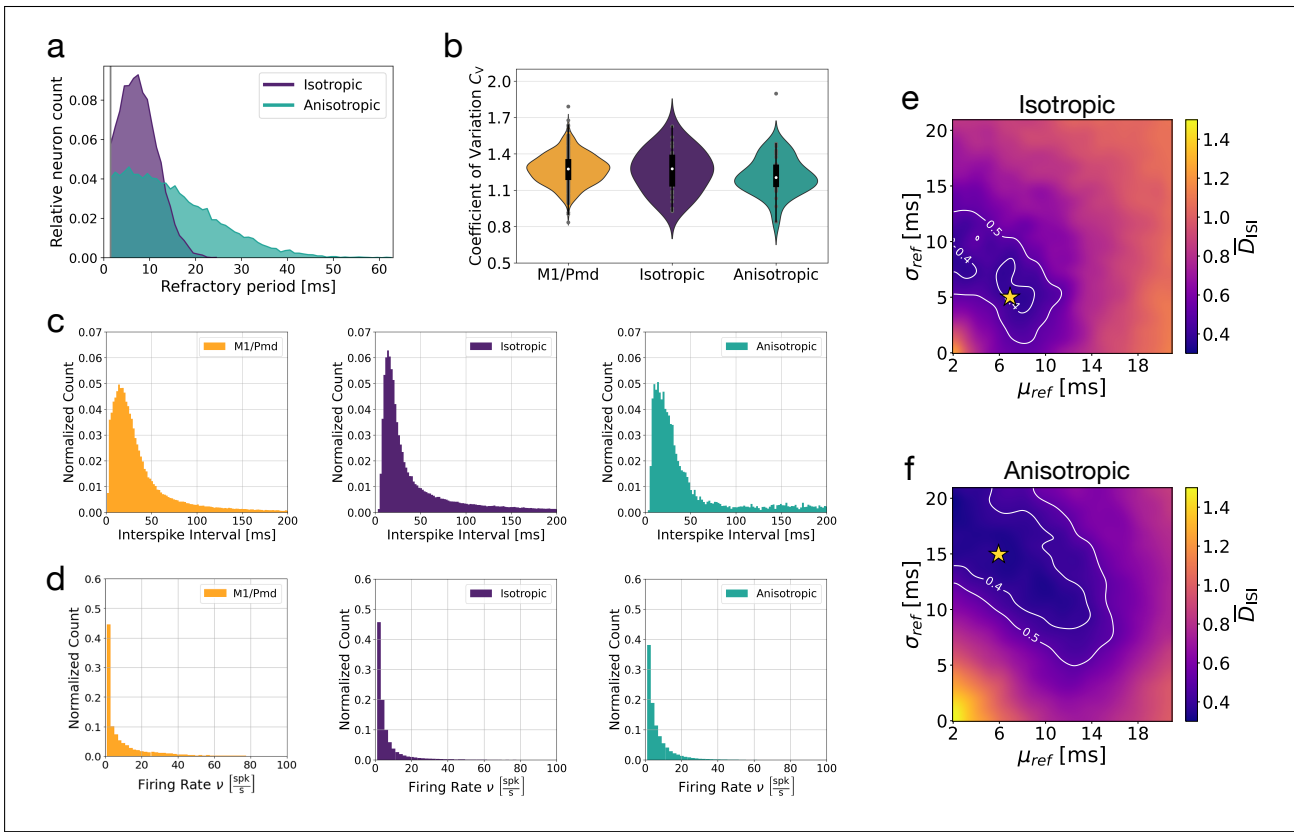


**Figure 4. Single neuron activity statistics in isotropic and anisotropic networks with heterogeneous neurons match experimental data.** (a) Example refractory period distributions for isotropic ( $\mu_\tau = 7$  ms,  $\sigma_\tau = 5$  ms) and anisotropic ( $\mu_\tau = 6$  ms,  $\sigma_\tau = 15$  ms) networks, see stars in (e) and (f). Normalized by number of excitatory neurons  $n_e = 14400$ . (b) Coefficient of variation for the M1/PMd data compared to the isotropic and anisotropic network simulations. (c) Interspike interval distributions for experimental data and network simulations. (d) Firing rate distributions for experimental data and network simulations. (e) Distance between the interspike interval distribution for the experimental data and isotropic network simulations as a function of the refractory period distribution ( $\mu_\tau, \sigma_\tau$ ). (f) Same as (e) but for the anisotropic network. Panels (a-d) correspond to stars in (e) and (f). CV, ISI, and firing rate distributions in (b,c,d) computed over 30 simulated networks, for experimental data over 489 trials. CV shows all data points (grey circles). CV median (white circle), interquartile range (black box), range (black line), kernel density estimate (violins) computed with data points  $> 3$  std. devs. removed. Parameter scan results in (e,f) averaged over 5 simulated networks. Smoothing and contour lines added for visualization.

137 in agreement. However, when refractory behavior was heterogeneous ( $\sigma_{ref}$  large enough), the  
 138 models and experimental data matched well and this was true for a range of refractory period  
 139 distributions ( $\mu_\tau, \sigma_\tau$ ). While both models fit the data, notably the anisotropic network did so  
 140 for a larger set of parameters (larger purple region, see contours) and for larger means  $\mu_\tau$  and  
 141 standard deviations  $\sigma_\tau$  (purple region and contours shifted up and to the right, compare Fig.

142 4f vs. 4e) meaning wider distributions with more heterogeneity in refractory behavior across  
143 neurons (Fig. 4a).

144 Fig. 4b,c,d shows an example fit (gold stars, Fig. 4e,f) for the isotropic and anisotropic models  
145 for the coefficient of variation, ISI distribution, and firing rate distribution. Neurons recorded  
146 from M1 and PMd have more variability in their firing patterns than a Poisson process, evidenced  
147 by a coefficient of variation larger than one. Both the isotropic and anisotropic models matched  
148 this spiking behavior (Fig. 4b). Likewise, the models reproduced the ISIs (Fig. 4c) and firing  
149 rates (Fig. 4d) observed in the data and the fit was confirmed by comparing with a different  
150 M1/PMd recording (Supplementary Fig. S2).

### 151 2.3 Neuronal network activity resulting from symmetric and corre- 152 lated asymmetric distance-dependent cortical connectivity

153 Next we were interested in the network activity of the isotropic and anisotropic models with  
154 parameters resulting from fitting both connectivity and activity statistics to cortical data. As  
155 discussed in the *Introduction*, while the isotropic network, with its symmetric connectivity, is  
156 expected to produce stationary activity bumps, the correlated asymmetric projections in the  
157 anisotropic network should give rise to spatiotemporal activity sequences. However, it remains  
158 unclear whether these findings hold true for the cortical parameter set.

159 Starting with the isotropic network model, we aimed to evoke intrinsically generated network  
160 activity under noisy background conditions. We conducted simulations in which a spatially  
161 localized burst of input was administered to the same network across 5 trials with different  
162 Gaussian white noise background input. The spatially localized burst varied on each trial, with  
163 a randomly selected 70% of the input region (404 of 576 neurons, a 24x24 neuron input region)  
164 receiving sufficient input current to spike at  $t_{\text{input}} = 10$  ms. We repeated this for 10 different  
165 networks each generated based on the distributions for connectivity ( $\sigma_{\text{loc,exc}} = 0.14$ ,  $p_{\text{con,rand}} = 0$ ,  
166 see Fig. 2c,e and Fig. 3b,d) and activity ( $\mu_\tau = 7$  ms,  $\sigma_\tau = 5$  ms, see Fig. 4e, gold star inside  
167 white contour) determined by the analyses in previous sections.

168 With symmetric distance-dependent connectivity and neuronal heterogeneity matched to exper-  
169 imental data, activity patterns in the isotropic network were dominated by spatially localized  
170 bumps (Fig. 5a,b). These activity bumps were transient with spatially local activity emerging  
171 and disappearing at different locations throughout the simulations (Fig. 5a,b). The pattern  
172 of transient emergence and disappearance was not consistent across trials as seen in the spike  
173 raster plots (Fig. 5a), activity plots of the two dimensional network topology (Fig. 5b), as  
174 well as when projected into low dimensional space (spanned by the first three principal com-

175 ponents) with neural trajectories showing inconsistent behavior (Fig. 5c). Notably, the level of  
 176 transience was variable across networks, with spatially localized activity at a particular location  
 177 sometimes remaining relatively persistent throughout the 500 ms simulation (Supplementary  
 178 Fig. S3).

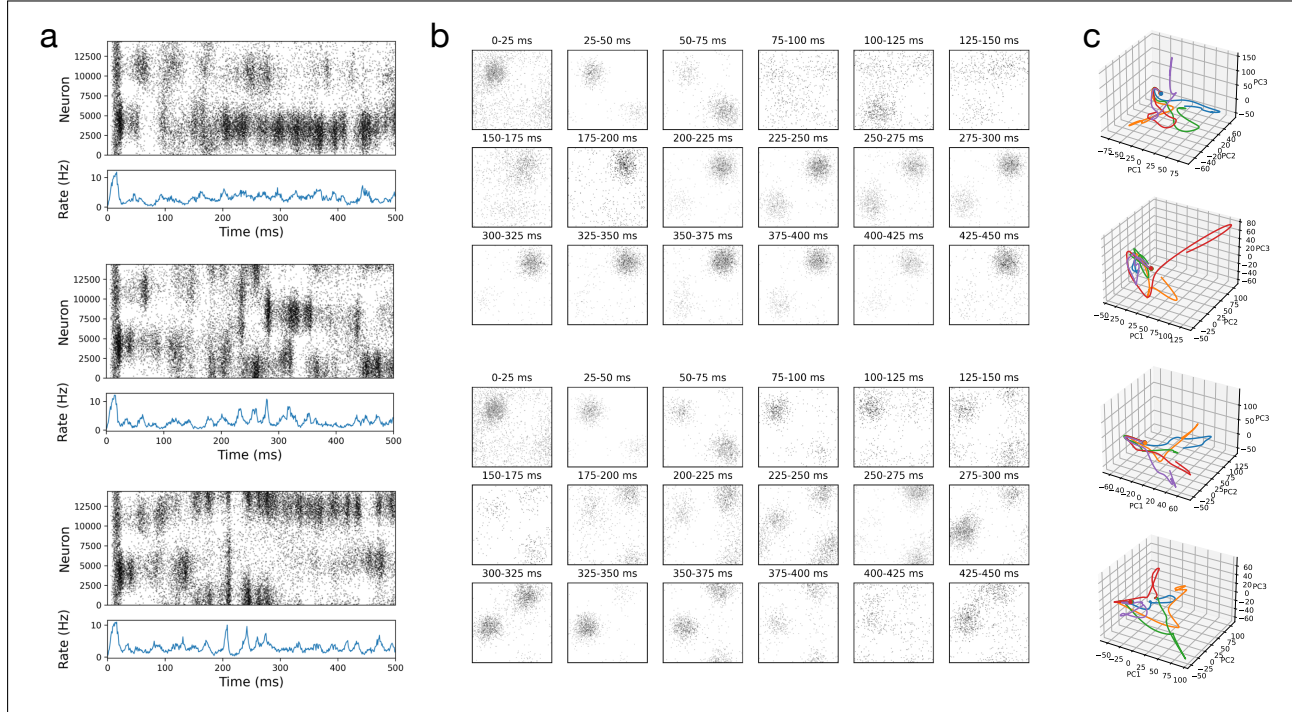


**Figure 5. Transient spatially localized activity in networks with symmetric distance-dependent connectivity.** (a) Three example trials depicting spiking behavior and average firing rates from the  $N = 14400$  excitatory neurons in the isotropic network. (b) Activity over time organized in 2D according to neuron position shows transient bumps of activity appear and disappear. Top and bottom correspond to top and bottom in (a) respectively. Example 2 from (a) not shown. (c) Projection onto the first three principal components. Each 3D plot shows 5 trials from different network simulations. Data from (a) and (b) correspond to trials from the top panel in (c).

179 Next we turned to the activity statistics of the anisotropically connected network model, where  
 180 we expect to find spatiotemporal activity sequences intrinsically generated by the correlated  
 181 asymmetries in neuronal projections. To evoke intrinsically generated network activity we stim-  
 182 ulated a spatially localized region (24x24 neurons) of the network across 5 trials with a randomly  
 183 selected subset of the region receiving input (404 of 576 neurons, 70%) and different Gaussian  
 184 white noise background input as before. We repeated this for 10 different anisotropically con-  
 185 nected networks each generated based on the distributions for connectivity ( $\sigma_{loc,exc} = 0.14$ ,  
 186  $p_{con,rand} = 0$ , see Fig. 2d,f and Fig. 3c,e) and activity ( $\mu_\tau = 6$  ms,  $\sigma_\tau = 15$  ms, see Fig. 4f, gold

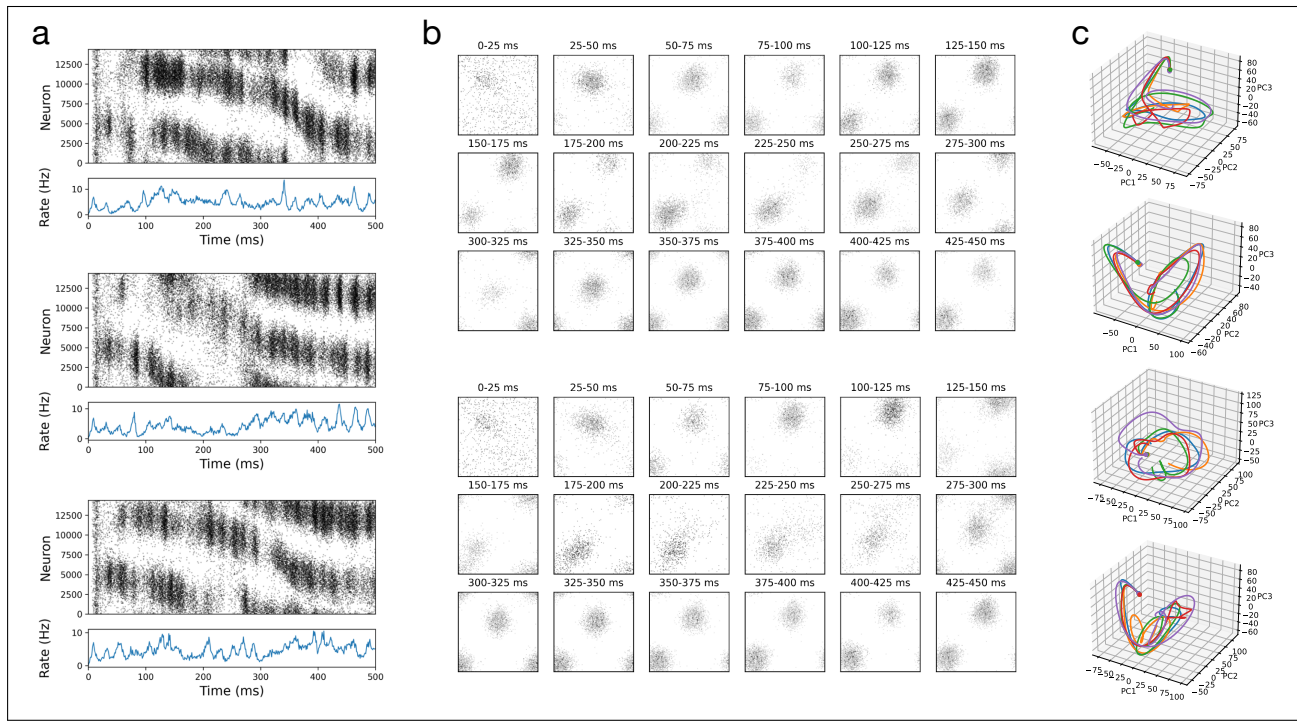


**Figure 6. Spatiotemporal activity sequences in network with correlated spatial asymmetries in distance-dependent connectivity.** (a) Three example trials depicting spiking behavior and average firing rates from the  $N = 14400$  excitatory neurons in the anisotropic network. (b) Activity over time organized in 2D according to neuron position shows spatiotemporal sequences of activity moving through the network. Top and bottom correspond to top and bottom in (a) respectively. Example 2 from (a) not shown. (c) Projection onto the first three principal components. Each 3D plot shows 5 trials from different network simulations. Data from (a) and (b) correspond to trials from the top panel in (c).

187 star inside white contour) determined by the analyses in previous sections.

188 In contrast to the transient but stationary spatially localized activity in the case of symmetric  
 189 distance-dependent connectivity, with correlated asymmetric projections we observed spatiotem-  
 190 poral sequences of activity (see Fig. 6). Activity patterns were again dominated by spatially  
 191 localized bumps (Fig. 6a,b) which in this case moved throughout the network (Fig. 6a,b). In  
 192 contrast with transient bumps in the isotropic case, spatiotemporal sequences showed consis-  
 193 tency across trials, with visibly similar spike trains (Fig. 6a), similar movement of spatially local  
 194 activity patterns (Fig. 6b), and accordingly, low dimensional neural trajectories that followed  
 195 similar paths (Fig. 6c).

196 Like the isotropic case, there was however variability across network simulations. We also  
 197 observed transient spatiotemporal sequences in which the spatially localized input triggered a  
 198 reliable initial response on the order of hundreds of milliseconds, after which point the activity

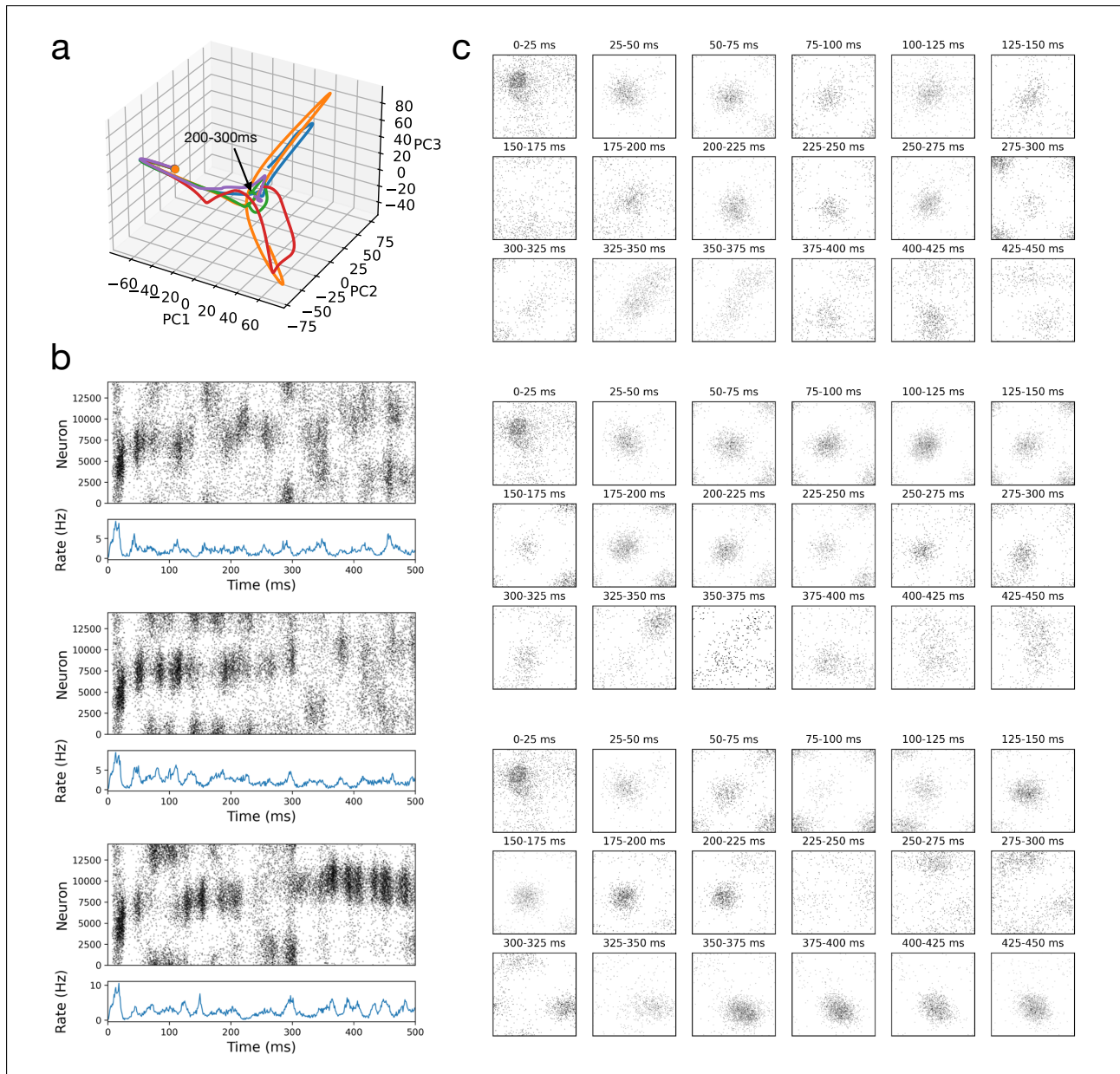


**Figure 7. Transient spatiotemporal sequences arise with correlated asymmetric connectivity.** (a) Projection of neural activity from five trials onto the first three principal components. Start of trial marked by dot. Trajectories follow the same path until they begin to diverge between 200 – 300 ms (black arrow). (b) Three example trials depicting spiking behavior and average firing rates from the  $N = 14400$  excitatory neurons in the anisotropic network during a transient spatiotemporal sequence (corresponding to green, purple, and red lines, respectively). (c) Activity over time organized in 2D according to neuron position. Top and bottom correspond to top and bottom in (b) respectively. A spatiotemporal sequence of activity moves slowly through the network with activity patterns becoming visibly different between 225 – 300 ms.

199 across trials diverged (Fig. 7). Fig. 7a shows a network simulation in which neural trajectories  
200 in 3D principal component space are tightly aligned for the first 200 – 300 ms after stimulation,  
201 before beginning to diverge. The transient response and divergence can be clearly observed in  
202 behavior of the bumps of activity moving through the two dimensional network topology (Fig.  
203 7c).

### 204 3 Discussion

205 Here we have shown that recurrent network models with distance-dependent connectivity match  
206 both microcircuit connectivity and activity statistics of cortical data from rat and monkey.  
207 Symmetric distance-dependent connectivity was sufficient to explain the pattern of two- and  
208 three-neuron connectivity motifs observed in rat visual cortex<sup>74</sup> (see also Miner and Triesch<sup>80</sup>).  
209 Surprisingly, introducing the assumption of asymmetric projections correlated in nearby neu-  
210 rons left the results unchanged, still fitting the nonrandom connectivity motifs. Likewise, single  
211 neuron activity statistics such as the distribution of firing rates, interspike intervals, and the  
212 coefficient of variation observed in monkey motor and premotor cortex could also be reproduced  
213 by both networks with distance-dependent symmetric as well as correlated asymmetric connec-  
214 tivity when heterogeneity in neuronal timescales was introduced via a distribution of refractory  
215 periods<sup>79</sup>.

216 With connectivity and neuronal timescales fitted to cortical data, both models produced spa-  
217 tially localized activity patterns in the 2D network topology. Symmetric connectivity gave  
218 rise to transient spatial patterns that emerged and disappeared, while correlated asymmetric  
219 connectivity produced spatiotemporal sequences of neuronal activity with spatially localized  
220 patterns becoming “unstuck in space”, and moving throughout the network.

221 Matching neuronal activity statistics from monkey motor/premotor cortex required different  
222 distributions of timescales depending on network connectivity. When connectivity was asym-  
223 metric and correlated, a wider distribution of timescales better fit the data (Fig. 4a). This  
224 result suggests that distributions of intrinsic timescales and refractory behavior may differ in  
225 brain regions that intrinsically generate spatiotemporal sequences compared with those that  
226 produce local transients. Notably, rhythmicity in firing rates emerged with heterogeneous re-  
227 fractory periods (Figs. 5-7), but how this relates to the precise shape of the refractory period  
228 distribution as well as the network level heterogeneity remains an open question.

229 Different to Spreizer et al.<sup>37</sup>, in the anisotropic network the parameters from fitting cortical data  
230 introduce a larger degree of variability in the network dynamics observed, with persisting spatial  
231 patterns, transient spatiotemporal sequences, and perturbations with spatiotemporal sequences

briefly following different paths on different trials (Figs. 5, 6, 7 and Supplementary Figs. S3, S4, S5). Given the multiple sources of noise, with variability in the spatially localized input (404 of 576 neurons, or 70% of the input region randomly receiving input on a given trial) as well as background noise, differences in network behavior are perhaps not surprising. Whether the source of variability lies in particulars of the network topology remains to be explored. Equally interesting may be the effect of plasticity, in particular for task learning, on the different types of observed network behavior.

The focus of our work was motivated by experimental data pointing to spatial asymmetries in distance-dependent cortical connectivity<sup>42–51</sup>, and past theoretical work linking these connectivity structures to sequence generation<sup>37</sup>. However there are a number of different accounts of sequence generation in recurrent networks. Proposals involve continuous attractors<sup>32,40</sup>, discrete attractors or cell assemblies connected in feedforward chains<sup>34,35,39</sup>, as well as symmetric distance-dependent connectivity with adaptation mechanisms<sup>28,30,32,36,81</sup> or distance-dependent transmission delays<sup>70</sup> enabling localized activity to propagate.

Our work lends further support to the notion that locally connected recurrent network models offer a parsimonious account of transient attractor-like activity as well as spatiotemporal sequences while requiring only few experimentally supported assumptions. Correlated asymmetries in the projection patterns of nearby neurons may be a key feature of cortical networks, enabling intrinsic generation of spatiotemporal activity sequences based on locally defined flows to produce rich and stable dynamics.

## 4 Materials and Methods

### 4.1 Software

Simulations were conducted with a custom software framework written in Python. The anisotropic network model code was based on an implementation by Leo Hiselius<sup>82</sup> in Brian2<sup>83</sup> with extended simulation management functionality inspired by the architecture from *PeleNet*<sup>84</sup>.

### 4.2 Neuron and synapse model

The model is based on Spreizer et al.<sup>37</sup> with a number of changes described below, see ref.<sup>37</sup> for additional information. The subthreshold membrane potential  $v(t)$  of a neuron in the network is modeled as

$$C_m \frac{dv}{dt} = -g_L(v(t) - E_L) + I(t) + \mu_{\text{GWN}} + \sigma_{\text{GWN}} \quad (1)$$

261 with the leak conductance  $g_L$ , the membrane capacitance  $C_m$ , the incoming current  $I(t)$ , the leak  
 262 potential  $E_L$ , and Gaussian white noise with mean  $\mu_{\text{GWN}}$  and standard deviation  $\sigma_{\text{GWN}}$ .

263 Synapses between neurons are described by the transient current  $I_{\text{syn}}$ , which is elicited by each  
 264 presynaptic spike as

$$I_{\text{syn}}(t) = J_{\text{syn}} \frac{t - (t_{\text{spk}} + t_{\text{delay}})}{\tau_{\text{syn}}} \exp\left(-\frac{t - (t_{\text{spk}} + t_{\text{delay}})}{\tau_{\text{syn}}}\right) H(t - (t_{\text{spk}} + t_{\text{delay}})) \quad (2)$$

265 with  $J_{\text{syn}}$  the synaptic strength,  $t_{\text{spk}}$  denotes the time of a spike in the presynaptic neuron,  $\tau_{\text{syn}}$  is  
 266 the time constant of the synapse,  $t_{\text{delay}}$  is the delay between presynaptic spike and post-synaptic  
 267 response, and  $H$  is the unit step function. The incoming synaptic current  $I_i(t)$  of neuron  $i$  at  
 268 time  $t$  is the sum over all the synaptic currents  $I_{\text{syn}}(t)$  that the neuron receives from its  $N_{\text{syn}}$   
 269 synapses at time  $t$ :

$$I_i(t) = \sum_{\text{syn}}^{N_{\text{syn}}} I_{\text{syn}}(t). \quad (3)$$

270 If  $v(t)$  reaches the threshold  $V_t$ , a spike event occurs at time  $t_{\text{spk}}$ . Spikes are transmitted from  
 271 pre- to post-synaptic neuron with delay time  $t_{\text{delay}}$ . After this event the neuron experiences an  
 272 absolute refractory period,  $\tau_{\text{ref}}$ . Following the spike the neuron's potential is reset to the resting  
 273 potential  $V_r$ . A spatially localized region of the network additionally receives a transient input  
 274 burst described below (see *Methods: Spatially local input*).

### 275 4.3 Neuron subpopulations and spatial organisation

276 We model a network of excitatory and inhibitory neurons (see EI-network, Spreizer et al. <sup>37</sup>),  
 277 with a ratio of four excitatory neurons to one inhibitory neuron based on cortical networks <sup>85</sup>.

278 When a presynaptic neuron is part of the excitatory subpopulation,  $J_{\text{syn}}$ , defined in Equation 3,  
 279 is equal to  $J_{\text{exc}} > 0$ , with excitatory synaptic strengths lognormally distributed (see *Methods:*  
 280 *Lognormal synaptic weight distribution*). For inhibitory presynaptic neurons  $J_{\text{syn}}$  is equal to  
 281  $J_{\text{inh}}$ , defined as:

$$J_{\text{inh}} = -J_{\text{exc}} \cdot g \quad (4)$$

282 with  $g$  being the strength of the inhibition. Both subpopulations of neurons are homogeneously  
 283 distributed on a square grid ( $x, y \in [0, 1]$ ) with periodic boundaries (i.e. the surface of a  
 284 toroid).

## 285 4.4 Interneuronal connectivity

286 Neurons form distance-dependent connections following a Gaussian distribution with a standard  
287 deviation  $\sigma_{loc,exc}$  for the projections of excitatory neurons and  $\sigma_{loc,inh}$  for the projections of  
288 inhibitory neurons. In the *anisotropic* network, for connections between excitatory neurons the  
289 center of this distribution is shifted away from the position of a neuron within the network,  
290 into a particular direction. This leads to a preferred axon direction  $\phi_i$  for each neuron. The  
291 magnitude of the shift is determined by the shift  $d$  and is equivalent for all neurons. For the  
292 *isotropic* network,  $d = 0$ .

293 The direction of the shift  $\phi_i$  is chosen individually for each neuron with Perlin noise, a gradient  
294 noise algorithm<sup>37,86</sup>. With this method, correlated directions are assigned to neurons that are  
295 close to each other. The result is an embedded local feedforward structure. Readers are referred  
296 to previous publications for further details<sup>37,38,86</sup>. Note that autapses are not permitted.

## 297 4.5 Lognormal synaptic weight distribution

298 In previous work, synaptic weights were equal for every synapse<sup>37,38</sup>. Here we assume a lognor-  
299 mal distribution of synaptic weights<sup>74,87,88</sup>. Weights are defined based on the distribution

$$J_{exc_{log}} = J_{exc} \cdot e^{\sigma_w \xi}, \quad (5)$$

300 with  $\xi$  being a normally distributed variable and  $J_{exc}$  being the original constant weight described  
301 in *Methods Neuron subpopulations and spatial organisation*.  $\sigma_w$  is a prefactor that scales the  
302 influence of the random variable. By setting  $\mu = \ln(J_{exc})$ , the resulting probability density  
303 function of the weights,  $p(J)$ , is defined as (see Fukai et al.<sup>89</sup>, Michaelis<sup>90</sup>)

$$p(J) = \frac{1}{\sigma_w J \sqrt{2\pi}} \cdot \exp\left(-\frac{(\ln(J) - \mu)^2}{2\sigma_w^2}\right). \quad (6)$$

304 Note, that  $\mu$  and  $\sigma_w$  are not the standard deviation and the mean of this distribution of  $J$  but  
305 rather of the distribution  $\ln(J)$ , since  $\ln(J)$  is normally distributed.

## 306 4.6 Spatially local input

307 A rectangular subset of the neuronal grid containing  $N_g$  excitatory neurons received spatially  
308 local input<sup>38</sup>. In particular, only a predefined share  $N_s \leq N_g$  of the neurons within this subset  
309 is stimulated with an instantaneous incoming current, strong enough to elicit a spike event at  
310 time  $t_{input}$ . This ignores temporal dynamics in the transient input burst.

311 The spatially local input arrived at a region of  $N_g = 576$  neurons (24x24 grid) of which on any  
312 given trial 70% ( $N_s = 404$ ) received input current leading them to spike at time  $t_{\text{input}} = 0.01s$ .  
313 For simulations with multiple trials (Figs. 5-7 and Supplementary Figs. S3-S5), the subset  
314 of  $N_s = 404$  neurons receiving input was randomly selected from the 24x24 neuron input  
315 region.

## 316 4.7 Distribution of refractory periods

317 Refractory periods were drawn from a Gaussian distribution

$$p(\tau_{\text{ref}}) = \frac{1}{\sqrt{2\pi}\sigma_\tau} e^{\frac{-(\tau_{\text{ref}}-\mu_\tau)^2}{2\sigma_\tau^2}}. \quad (7)$$

318 Here  $\sigma_\tau$  is the standard deviation and  $\mu_\tau$  is the average of the distribution of  $\tau_{\text{ref}}$ . The probability  
319 that a neuron has a refractory period equal to  $\tau_{\text{ref}}$  is, therefore,  $p(\tau_{\text{ref}})$ . Different locations of  
320 stimulation within a single neuron can lead to different refractory periods<sup>79</sup>, but for this work  
321 each neuron's refractory period remains fixed.

322 We considered refractory period distributions with  $\mu_\tau \in [2\text{ ms}, 20\text{ ms}]$  and  $\sigma_\tau \in [0\text{ ms}, 20\text{ ms}]$ .  
323 To exclude the possibility of negative and very small refractory periods the Gaussian distribu-  
324 tion is cut at 1.5 milliseconds and capped at 120 milliseconds to avoid arbitrarily large  $\tau_{\text{ref}}$ .  
325 We performed a parameter search over the mean and standard deviation of the refractory pe-  
326 riod distribution to fit single neuron activity statistics of the experimental data (Fig. 4 and  
327 Supplementary Fig. S2).

## 328 4.8 Connectivity motifs

329 We compared the recurrent connectivity in the *anisotropic* and *isotropic* network models to  
330 data from layer 5 pyramidal neurons in rat visual cortex<sup>74</sup>. Song et al.<sup>74</sup> considered connectivity  
331 motifs of pairs and triads of recorded neurons and found the distributions differed from what is to  
332 be expected in a randomly connected network. For neuronal pairs there are three possible motifs,  
333 namely they can be connected bidirectionally, unidirectionally or not connected at all (Fig. 2a).  
334 For groups of three neurons, there are 16 different possible motifs (Fig. 3a). In the nomenclature  
335 of the three neuron motifs, the first digit represents the overall bidirectional connections, the  
336 second digit represents unidirectional connections and the third missing connections respectively.  
337 D, U and C refer to certain patterns arising from the directionality of the connections.

338 For the model, the probability  $p_{\text{con}} = 0.116$  of a connection between two neurons is chosen such  
339 that it equals the experimental finding in Song et al.<sup>74</sup>. This probability is used in the synaptic

340 initialisation processes of both excitatory and inhibitory neuron subpopulations.

341 Based on the connection probability, Song et al. <sup>74</sup> calculated the probability of the different  
342 motifs under the assumption that the network is randomly connected. They compared these  
343 expected values to the experimentally observed motif counts and found a pattern of over- and  
344 underrepresentations of single motifs in the network beyond what is expected in a randomly con-  
345 nected network. Here we applied the same comparison to the motifs of synaptic connections in  
346 the model, which result from the connectivity generating rules described in *Methods: Interneu-*  
347 *ronal connectivity*. To determine the role of the anisotropy of the models synaptic connections,  
348 we evaluated the same statistics for a model without a shift in its connectivity (i.e.  $d = 0$ ,  
349 see *Methods: Interneuronal connectivity*), the isotropic model. In this version the locality of  
350 the connectivity is preserved but neurons project symmetrically in all directions, thus lacking  
351 correlated anisotropy.

352 To quantify the distribution of motifs we split all neurons of the respective model randomly into  
353 pairs and counted the respective directed connections using their weight matrices. We repeated  
354 this procedure for neuronal triads. Every neuron was sampled only once for a pair and once for  
355 a triad.

356 We computed two and three neuron motif distributions as a function of two parameters. The  
357 connection locality  $\sigma_{loc,exc}$ , i.e. the standard deviation of the Gaussian kernel for excitatory con-  
358 nections, was varied in the range  $\sigma_{loc,exc} \in [0.01, 0.25]$  and the proportion of random connections  
359  $p_{con,rand}$  was varied in the range  $p_{con,rand} \in [0, 0.25]$ . Random connections are those not restricted  
360 to the local neighborhood of a neuron defined by  $\sigma_{loc,exc}$ . The random connections replace local  
361 connections, hence the overall connection probability remains preserved. Note  $p_{con,rand} = 0$  is a  
362 purely locally connected network and e.g.  $p_{con,rand} = 0.25$  means that 25% of connections are  
363 randomly distributed and 75% of connections are local.

364 In the first step of the motif evaluation we estimated the occurrence  $n_{occ}$  of each motif (3  
365 for two neuron motifs, 16 for three neuron motifs) within the respective number of neuron  
366 groups with size  $n_{group}$ . With 14400 excitatory neurons in the model, sampling all neurons  
367 leads to  $n_{group}$  equalling 7200 samples for neuron pairs and 4800 samples for triads of neurons.  
368 We then calculated the relative representation  $r_{rel}$  for each motif by dividing the observed  
369 occurrence  $n_{occ}$  by its expected occurrence under the assumption of a random connectivity, as  
370 it was performed by Song et al. <sup>74</sup>. The expected occurrence can be determined by the overall  
371 number of analysed neurons groups  $n_{group}$  times the probability  $p_{motif}$  of the motif in a randomly

372 connected network

$$r_{\text{rel}} = \frac{n_{\text{occ}}}{n_{\text{group}} \cdot p_{\text{random}}}. \quad (8)$$

373 The probabilities  $p_{\text{motif}}$  for the different motifs are listed in Table 1 for two-neuron motifs  
 374 and Table 2 for three-neuron motifs. They depend on the overall connection probability of  
 375 two neurons  $p_{\text{con}}$  equal to 11.6% in the model, which is the connection probability from the  
 experimental data<sup>74</sup>.

Motif	$p_{\text{motif}}$
$p_{\text{uni}}$ (Unidirectional)	$2 \cdot (p_{\text{con}}(1 - p_{\text{con}}))$
$p_{\text{bi}}$ (Bidirectional)	$p_{\text{con}}^2$
$p_{\text{none}}$ (No connection)	$(1 - p_{\text{con}})^2$

**Table 1.** Probabilities of two neuron motifs expected in a randomly connected network.

376

Motif	$p_{\text{motif}}$
<b>012</b>	$6 \cdot (p_{\text{none}}^2) \cdot p_{\text{uni}}$
<b>102</b>	$3 \cdot (p_{\text{none}}^2) p_{\text{bi}}$
<b>021D</b>	$3 \cdot p_{\text{none}} \cdot p_{\text{uni}}^2$
<b>021U</b>	$3 \cdot p_{\text{none}} \cdot p_{\text{uni}}^2$
<b>021C</b>	$6 \cdot p_{\text{none}} \cdot p_{\text{uni}}^2$
<b>111D</b>	$6 \cdot p_{\text{none}} \cdot p_{\text{uni}} \cdot p_{\text{bi}}$
<b>111U</b>	$6 \cdot p_{\text{none}} \cdot p_{\text{uni}} \cdot p_{\text{bi}}$
<b>201</b>	$3 \cdot p_{\text{none}} \cdot p_{\text{bi}}^2$
<b>030T</b>	$6 \cdot p_{\text{uni}}^3$
<b>030C</b>	$2 \cdot p_{\text{uni}}^3$
<b>120D</b>	$3 \cdot (p_{\text{uni}}^2) \cdot p_{\text{bi}}$
<b>120C</b>	$6 \cdot (p_{\text{uni}}^2) \cdot p_{\text{bi}}$
<b>120U</b>	$3 \cdot (p_{\text{uni}}^2) \cdot p_{\text{bi}}$
<b>210</b>	$6 \cdot p_{\text{uni}} \cdot p_{\text{bi}}^2$
<b>300</b>	$1 \cdot p_{\text{bi}}^3$

**Table 2.** Probabilities of three-neuron motifs expected in a randomly connected network depending of the probabilities of two-neuron motifs  $p_{\text{uni}}, p_{\text{bi}}, p_{\text{none}}$ .

377 To estimate  $p_{\text{motif}}$  for the three neuron motifs, Song et al.<sup>74</sup> did not use  $p_{\text{uni}}, p_{\text{bi}}$  and  $p_{\text{none}}$  as  
 378 they would be expected in a random network, but rather the probability of occurrence of two-  
 379 neuron motifs they observed for the rat visual cortex neurons. The reason is to ensure that  
 380 overrepresented three-neuron patterns are not spuriously detected simply because they contain  
 381 an overrepresented two-neuron pattern. We apply the same approach using  $p_{\text{uni}}, p_{\text{bi}}$  and  $p_{\text{none}}$   
 382 from the experimental data<sup>74</sup>.

383 For each parameter set ( $\sigma_{loc,exc}$ ,  $p_{con,rand}$ ), we estimated the average over  $N_{seed}=5$  different net-  
 384 work initialisations generated by using different random seeds for the connectivity. In the  
 385 anisotropic model every initialisation has a different landscape of preferred directions (see *Meth-  
 386 ods: Interneuronal connectivity*) as well as a different initial pseudorandom number generator  
 387 state for the process of the determination of synaptic connections based on  $p_{con}$  within the  
 388 model. Since there is no preferred direction in the isotropic model only the latter changes  
 389 within its initialisations.

390 The mean relative representation  $\bar{r}_{rel_j}$  of a motif  $j$  for a certain parameter set is computed  
 391 as

$$\bar{r}_{rel_j} = \frac{\bar{n}_{occ_j}}{n_{group} \cdot p_{random_j}} \quad (9)$$

392 with  $\bar{n}_{occ_j}$ , the mean occurrence of every motif, defined as

$$\bar{n}_{occ_j} = \frac{1}{N_{seed}} \sum_i^{N_{seed}} n_{occ_{i,j}}. \quad (10)$$

393 To estimate the deviation  $e_{r_j}$  of the relative representation  $\bar{r}_{rel,model_j}$  of a motif  $j$  from the  
 394 model to the relative representation  $r_{rel,exp_j}$  of the same motif  $j$  in the experimental data<sup>74</sup>, we  
 395 calculated the absolute value of their difference and normalised it by the relative representation  
 396 within the experimental data  $r_{rel,exp_j}$

$$e_{r_j} = \frac{|\bar{r}_{rel,model_j} - r_{rel,exp_j}|}{r_{rel,exp_j}}. \quad (11)$$

397 In order to have a measure to compare the match between the model motifs and the motifs  
 398 from the experimental data for many sets of parameters, we averaged the  $e_{r_j}$  for the different  
 399 motifs of two neuron motifs ( $N_{motif} = 3$ ) as well as for three neuron motifs ( $N_{motif} = 16$ ) giving  
 400 the *mean relative error*  $E_r$ , defined as:

$$E_r = \frac{1}{N_{motif}} \sum_j^{N_{motif}} e_{r_j}. \quad (12)$$

## 401 4.9 Electrophysiological data

402 Methodological details relating to recording, waveform identification, and offline sorting are  
403 provided in the methods of previous work<sup>91</sup> for neural recordings from macaque monkey cortical  
404 areas PMd and M1 via floating microelectrode arrays (128-channels total; 64-channels per area).  
405 In this paper, we make use of similar data from a memory-guided center-out reach task to one  
406 of four directions (0°, 90°, 180°, 270°, pseudo-randomly interleaved from trial to trial), which  
407 was collected for another project (Nowak, Morel & Gail, unpublished).

408 Data from two different recording sessions (referred to as DS1 and DS2) were analyzed for  
409 reliability, the first with 66 neurons and the second with 56 neurons (in M1 and PMd combined).  
410 We considered only trials in which the monkey successfully performed the task for analysis (489  
411 and 438 successful trials, respectively). For each trial, we considered spiking data in the time  
412 window from instruction to initiate the movement until the movement end(duration, mean ±  
413 standard deviation for DS1: 575.60±76.05 milliseconds; DS2 568.18±89.65 milliseconds).

## 414 4.10 Neuronal activity measures

415 We compared single neuron activity statistics from the electrophysiological data to simulations of  
416 *anisotropically* and *isotropically* connected network models in response to a transient spatially  
417 local burst of input (see *Methods: Spatially local input*) with background noise. Here we varied  
418 the mean and standard deviation of the refractory period distribution (see *Methods: Distribution*  
419 *of refractory periods*) and quantified firing rates, interspike intervals, and the coefficient of  
420 variation.

### 421 4.10.1 Neuronal firing rates

422 The firing rate  $\nu_i$  of a neuron  $i$  is computed by dividing the number of spikes  $n_{\text{spk}}$  by the  
423 evaluated time interval  $T$

$$\nu_i = \frac{n_{\text{spk}}}{T}. \quad (13)$$

424 We compared the distribution of firing rates in simulations with the experimental data (see  
425 *Methods: Comparison of distributions*).

#### 426 4.10.2 Interspike intervals

427 An interspike interval (ISI) measures the time interval  $s_k$  in between two subsequent spikes  $\text{spk}_k$   
428 and  $\text{spk}_{k+1}$  of a neuron:

$$s_k = t_{\text{spk}_k} - t_{\text{spk}_{k+1}}. \quad (14)$$

429 We quantified the distribution of ISIs across neurons. Details on this analysis can be found in  
430 *Methods: Comparison of distributions*.

#### 431 4.10.3 Coefficient of variation

432 The coefficient of variation ( $C_V$ ) measures the regularity of a spike train compared to a spike  
433 train that would arise from a Poisson process<sup>92</sup>. In a Poisson process neurons have a constant  
434 firing rate  $\nu$  and spikes occur independently and stochastically<sup>92</sup>, based on  $\nu$ . Therefore the  
435 average number of spikes in the interval  $T$  is  $\nu \cdot T$ . The coefficient of variation for a Poisson  
436 process is equal to 1 ( $C_V = 1$ ). It holds that  $C_V < 1$  if the spike train is more regular and  
437  $C_V > 1$  if it is less regular than a Poisson process<sup>92</sup>.  $C_V$  is estimated by the division of the  
438 standard deviation of ISIs,  $\sigma_{\text{ISI}}$ , of a spike train by the expected value of the ISIs,  $\mu_{\text{ISI}}$ , of the  
439 same spike train

$$C_V = \frac{\sigma_{\text{ISI}}}{\mu_{\text{ISI}}}. \quad (15)$$

### 440 4.11 Comparison of distributions

#### 441 4.11.1 Binning of ISIs and firing rates

442 We binned and normalized the ISIs and firing rates for comparison between experimental and  
443 simulated data. For ISI distributions, data was binned into  $N_{\text{bin}} = 100$  bins covering a range of  
444 ISIs between 0 ms and 200 ms and the width of each bin was  $w_b = 2$  milliseconds. For the firing  
445 rates,  $N_{\text{bin}} = 50$  bins were calculated ranging from 0 Hz to 100 Hz with  $w_b = 2$  Hz. Neurons  
446 with less than one spike in a trial were not considered for firing rate distributions and those  
447 with less than 2 spikes were not considered for ISI distributions.

448 For the experimental data, in DS1  $N_{\text{sample}} = 66$  neurons were recorded over  $N_{\text{trials}} = 489$  trials  
449 and in DS2  $N_{\text{sample}} = 56$  neurons were recorded over  $N_{\text{trials}} = 438$  trials. Bins are normalised  
450 by dividing them by the number of neurons times the number of trials.

451 In the simulation data, for each simulation we sampled  $N_{\text{sample}} = 2000$  neurons. Fig. 4b-d and  
452 Supplementary Fig. S2a-c show binned data for  $N_{\text{seed}} = 30$  simulations and the comparisons

453 in Fig. 4e,f and Supplementary Fig. S2d,e are averages over  $N_{\text{seed}} = 5$  simulations. This  
454 means for the former, ISIs and firing rates from the  $N_{\text{seed}} = 30$  were binned together and  
455 normalized by  $N_{\text{sample}} \cdot N_{\text{seed}}$ , and for the latter each simulation was normalized separately and  
456 then averaged.

#### 457 4.11.2 Differences between distributions

458 To estimate the differences between model and experimental distributions we calculated the  
459 differences  $d_i$  of every bin  $b_{i_{\text{mod}}}$  in the model to its counterpart in the experimental data  $b_{i_{\text{exp}}}$ .  
460 The absolute value of the difference is taken to compare the magnitude of the deviation. The  
461 difference measure is given by

$$d_i = |b_{i_{\text{mod}}} - b_{i_{\text{exp}}}|. \quad (16)$$

462 The  $N_{\text{bin}}$  bin-differences of a single network initialisation are summed up and an average of this  
463 sum is taken from the five initialisations. This results in the mean distribution difference of ISI  
464 distributions  $\overline{D}_{\text{ISI}}$

$$\overline{D}_{\text{ISI}} = \frac{1}{N_{\text{seed}}} \sum_j^{N_{\text{seed}}} \sum_i^{N_{\text{bin}}} d_{j,i}. \quad (17)$$

465 The comparison of ISI distributions between the models and DS1 is shown in Fig. 4e,f and with  
466 DS2 in Supplementary Fig. S2d,e.

#### 467 4.12 Stimulus-evoked activity

468 For the stimulus-evoked activity, neurons were initialized at their rest potential and an instanta-  
469 neous spatially localized input was administered at  $t = 10$  ms during ongoing background input  
470 (see *Methods: Spatially local input*). Simulations lasted 500 ms with time step 0.1 ms. For  
471 activity statistics comparisons, we repeated the stimulus-evoked measurements for five different  
472 network initialisations for Fig. 4e,f and Supplementary Fig. S2d,e and for 30 initialisations for  
473 Fig. 4b-d and Supplementary Fig. S2a-c.

474 To assess transient bump vs. spatiotemporal sequences, we considered 10 different networks  
475 initialisations. In this case, in the same network five trials were conducted with stimulation  
476 delivered to a randomly selected 70% of the input region (404 of 576 neurons, a 24x24 neuron  
477 input region) as described before.

478 **4.12.1 Spike rasters**

479 Spike raster plots show all spikes for all excitatory neurons with neuron order simply being the  
480 2D network topology unrolled into a 1D vector.

481 **4.12.2 Instantaneous firing rates**

Instantaneous firing rate plots were made by temporally binning spikes from all  $n_e = 14400$  excitatory neurons into 1 ms bins and dividing the number of spikes in a temporal bin  $i$ ,  $n_{spks}(\Delta t_i)$ , by the bin size  $\Delta t_i$  and number of neurons  $n_e$ . In a formula:

$$R(\Delta t_i) := \frac{n_{spks}(\Delta t_i)}{n_e \cdot \Delta t_i}.$$

482 **4.12.3 2D activity plots**

483 For 2D activity plots we simply plotted a black dot at the location in the 2D network topology  
484 for each spike that occurred within a given 25 ms temporal window.

485 **4.12.4 Principal component analysis**

486 Spike data was binned into 1 ms bins resulting in a 14400x500 matrix containing spikes for  $n_e$   
487 excitatory neurons for each time bin. The data was smoothed by convolving the spike train of  
488 each neuron with a Gaussian with temporal standard deviation 25 ms (using Python method  
489 `numpy.convolve` with `mode="same"`). For the 5 trials from a single network, the smoothed spike  
490 rasters were concatenated into a 14400x2500 dimensional matrix. Each neuron's smoothed spike  
491 train was centered and scaled to unit variance (using `sklearn.preprocessing.StandardScaler`).  
492 Principal component analysis was applied to the resulting matrix (using `sklearn.decomposition`  
493 `PCA`) and the smoothed, centered, and scaled spike raster was projected onto the first three  
494 principal components giving a matrix of size 3x2500. We separated the matrix back into the  
495 constituent trials (5 trials of 3x500) and plotted them in 3D.

496 **4.13 Smoothing data for visualisation**

497 For parameter search figures comparing model and experimental data for both the connec-  
498 tivity and activity statistics, we used a Gaussian filter with  $\sigma = 0.7$  to smooth the data using  
499 `scipy.ndimage.gaussian_filter` and upsampled by a factor of 10 using `scipy.ndimage.zoom`.

## 500 4.14 Parameters

501 If not stated differently the following parameters of the model used in this work was defined as  
following. For the isotropic network model  $d_{\text{shift}}$  was set to 0.

Parameter	Value
$C_m$	$250 \text{ pF}$
$g_L$	$25 \text{ nSiemens}$
$E_L$	$-70 \text{ mV}$
$V_t$	$-55 \text{ mV}$
$V_r$	$-70 \text{ mV}$
$\tau_m$	$\frac{C_m}{g_L}$
$\mu_{\text{GWN}}$	$250 \text{ pA}$
$\sigma_{\text{GWN}}$	$85 \text{ pA}$
$g$	7
$\tau_{\text{ref}}$	$[1.5, 120] \text{ ms}$
$\tau_e$	$5 \text{ ms}$
$\tau_i$	$5 \text{ ms}$

**Table 3.** Neuron parameters

502

Parameter	Value
$J_{\text{exc}}$	$10 \cdot e \text{ pA}$
$J_{\text{inh}}$	$-g \cdot J_{\text{exc}}$
$\sigma_{\text{loc,exc}}$	0.14
$\sigma_{\text{loc,inh}}$	$\frac{\sigma_{\text{loc,exc}}}{0.75}$
$t_{\text{delay}}$	$1 \text{ ms}$
$p_{\text{con,exc}}$	0.116
$p_{\text{con,inh}}$	0.116
$s_{\text{perlin}}$	2
$d_{\text{shift}}$	1
$p_{\text{con,rand}}$	0

**Table 4.** Synaptic parameters

Parameter	Value
$t_{\text{simulation}}$	$0.5 \text{ s}$
$t_{\text{input}}$	$0.01 \text{ s}$
$n_e$	14400
$n_i$	3600

**Table 5.** Network and simulation parameters

## 503 5 Author contributions

504 Conceptualization ABL FE CM AK CT Data Curation ABL FE CM JN AG Formal Analysis  
505 ABL FE CM Funding Acquisition ABL AK AG CT Investigation ABL FE CM JN Method-  
506 ology ABL FE CM Project Administration ABL CM Resources AG, CT Software FE ABL  
507 CM Supervision AK CT Validation ABL FE CM Visualization ABL FE CM Original Draft  
508 Preparation ABL FE Review & Editing ABL FE CM JN AG AK CT.

## 509 6 Acknowledgements

510 We thank Leo Hiselius for making his code publicly available and for discussions related to his  
511 code. We thank Benjamin Schulz for programming work related to the motif analysis. This  
512 work was supported by the German Research Foundation (Deutsche Forschungsgemeinschaft) in  
513 the context of the SFB 889 'Cellular Mechanisms of Sensory Processing' (C4) and the European  
514 Commission in the context of the Plan4Act consortium (Grant H2020-FETPROACT-16 732266;  
515 project WP1), as well as the Swedish Research Council and StratNeuro. ABL is supported by  
516 a Natural Sciences and Engineering Research Council of Canada PGSD-3 scholarship.

## 517 References

- 518 [1] Christopher D Harvey, Philip Coen, and David W Tank. Choice-specific sequences in  
519 parietal cortex during a virtual-navigation decision task. *Nature*, 484(7392):62–68, 2012.
- 520 [2] Dezhe Z Jin, Naotaka Fujii, and Ann M Graybiel. Neural representation of time in cortico-  
521 basal ganglia circuits. *Proceedings of the National Academy of Sciences*, 106(45):19156–  
522 19161, 2009.
- 523 [3] Konstantin I Bakhurin, Vishwa Goudar, Justin L Shobe, Leslie D Claar, Dean V Buono-  
524 mano, and Sotiris C Masmanidis. Differential encoding of time by prefrontal and striatal  
525 network dynamics. *Journal of Neuroscience*, 37(4):854–870, 2017.
- 526 [4] Christopher J MacDonald, Kyle Q Lepage, Uri T Eden, and Howard Eichenbaum. Hippo-  
527 campal “time cells” bridge the gap in memory for discontiguous events. *Neuron*, 71(4):  
528 737–749, 2011.
- 529 [5] Rainer W Friedrich and Gilles Laurent. Dynamic optimization of odor representations by  
530 slow temporal patterning of mitral cell activity. *Science*, 291(5505):889–894, 2001.

- 531 [6] Richard HR Hahnloser, Alexay A Kozhevnikov, and Michale S Fee. An ultra-sparse code  
532 underlies the generation of neural sequences in a songbird. *Nature*, 419(6902):65–70, 2002.
- 533 [7] Henrik Lindén, Peter C Petersen, Mikkel Vestergaard, and Rune W Berg. Movement is  
534 governed by rotational neural dynamics in spinal motor networks. *Nature*, 610(7932):526–  
535 531, 2022.
- 536 [8] Juan A Gallego, Matthew G Perich, Stephanie N Naufel, Christian Ethier, Sara A Solla,  
537 and Lee E Miller. Cortical population activity within a preserved neural manifold underlies  
538 multiple motor behaviors. *Nature communications*, 9(1):4233, 2018.
- 539 [9] Jean-Baptiste Eichenlaub, Beata Jarosiewicz, Jad Saab, Brian Franco, Jessica Kelemen,  
540 Eric Halgren, Leigh R Hochberg, and Sydney S Cash. Replay of learned neural firing  
541 sequences during rest in human motor cortex. *Cell Reports*, 31(5):107581, 2020.
- 542 [10] William E Skaggs and Bruce L McNaughton. Theta phase precession in hippocampal.  
543 *Hippocampus*, 6:149–172, 1996.
- 544 [11] Eva Pastalkova, Vladimir Itskov, Asuhan Amarasingham, and Gyorgy Buzsaki. Internally  
545 generated cell assembly sequences in the rat hippocampus. *Science*, 321(5894):1322–1327,  
546 2008.
- 547 [12] György Buzsáki and David Tingley. Space and time: the hippocampus as a sequence  
548 generator. *Trends in cognitive sciences*, 22(10):853–869, 2018.
- 549 [13] John O’Keefe. Place units in the hippocampus of the freely moving rat. *Experimental  
550 Neurology*, 51(1):78–109, 1976.
- 551 [14] George Dragoi and György Buzsáki. Temporal encoding of place sequences by hippocampal  
552 cell assemblies. *Neuron*, 50(1):145–157, 2006.
- 553 [15] David J Foster and Matthew A Wilson. Reverse replay of behavioural sequences in hip-  
554 pocampal place cells during the awake state. *Nature*, 440(7084):680, 2006.
- 555 [16] Kamran Diba and György Buzsáki. Forward and reverse hippocampal place-cell sequences  
556 during ripples. *Nature Neuroscience*, 10(10):1241, 2007.
- 557 [17] Mehrab N Modi, Ashesh K Dhawale, and Upinder S Bhalla. Ca1 cell activity sequences  
558 emerge after reorganization of network correlation structure during associative learning.  
559 *Elife*, 3:e01982, 2014.
- 560 [18] Sen Cheng. The crisp theory of hippocampal function in episodic memory. *Frontiers in  
561 neural circuits*, 7:88, 2013.

- 562 [19] Upinder S Bhalla. Dendrites, deep learning, and sequences in the hippocampus. *Hippocampus*-  
563 *pus*, 29(3):239–251, 2019.
- 564 [20] Soledad Gonzalo Cogno, Horst A Obenhaus, Ane Lautrup, R Irene Jacobsen, Claudia  
565 Clopath, Sebastian O Andersson, Flavio Donato, May-Britt Moser, and Edvard I Moser.  
566 Minute-scale oscillatory sequences in medial entorhinal cortex. *Nature*, pages 1–7, 2023.
- 567 [21] Artur Luczak, Peter Barthó, Stephan L Marguet, György Buzsáki, and Kenneth D Harris.  
568 Sequential structure of neocortical spontaneous activity in vivo. *Proceedings of the National  
569 Academy of Sciences*, 104(1):347–352, 2007.
- 570 [22] Shun-ichi Amari. Dynamics of pattern formation in lateral-inhibition type neural fields.  
571 *Biological cybernetics*, 27(2):77–87, 1977.
- 572 [23] Hans-Martin R Arnoldi and Wilfried Brauer. Synchronization without oscillatory neurons.  
573 *Biological Cybernetics*, 74(3):209–223, 1996.
- 574 [24] John Hertz. Modelling synfire processing. 1997.
- 575 [25] Markus Diesmann, Marc-Oliver Gewaltig, and Ad Aertsen. Stable propagation of syn-  
576 chronous spiking in cortical neural networks. *Nature*, 402(6761):529–533, 1999.
- 577 [26] Moshe Abeles, Gaby Hayon, and Daniel Lehmann. Modeling compositionality by dynamic  
578 binding of synfire chains. *Journal of Computational Neuroscience*, 17(2):179–201, 2004.
- 579 [27] Arvind Kumar, Stefan Rotter, and Ad Aertsen. Conditions for propagating synchronous  
580 spiking and asynchronous firing rates in a cortical network model. *Journal of Neuroscience*,  
581 28(20):5268–5280, 2008.
- 582 [28] Lawrence Christopher York and Mark CW van Rossum. Recurrent networks with short  
583 term synaptic depression. *Journal of computational neuroscience*, 27(3):607, 2009.
- 584 [29] Ila R Fiete, Walter Senn, Claude ZH Wang, and Richard HR Hahnloser. Spike-time-  
585 dependent plasticity and heterosynaptic competition organize networks to produce long  
586 scale-free sequences of neural activity. *Neuron*, 65(4):563–576, 2010.
- 587 [30] Vladimir Itskov, Carina Curto, Eva Pastalkova, and György Buzsáki. Cell assembly se-  
588 quences arising from spike threshold adaptation keep track of time in the hippocampus.  
589 *Journal of Neuroscience*, 31(8):2828–2834, 2011.
- 590 [31] Yao Lu, Yuzuru Sato, and Shun-ichi Amari. Traveling bumps and their collisions in a  
591 two-dimensional neural field. *Neural Computation*, 23(5):1248–1260, 2011.

- 592 [32] Amir H Azizi, Laurenz Wiskott, and Sen Cheng. A computational model for preplay in  
593 the hippocampus. *Frontiers in computational neuroscience*, 7:161, 2013.
- 594 [33] David Kappel, Bernhard Nessler, and Wolfgang Maass. STDP installs in winner-take-all  
595 circuits an online approximation to hidden Markov model learning. *PLOS Computational  
596 Biology*, 10(3), 2014.
- 597 [34] Nikolay Chenkov, Henning Sprekeler, and Richard Kempter. Memory replay in balanced  
598 recurrent networks. *PLoS computational biology*, 13(1):e1005359, 2017.
- 599 [35] James M Murray et al. Learning multiple variable-speed sequences in striatum via cortical  
600 tutoring. *eLife*, 6:e26084, 2017.
- 601 [36] Alexander Seeholzer, Moritz Deger, and Wulfram Gerstner. Stability of working memory  
602 in continuous attractor networks under the control of short-term plasticity. *PLoS computational  
603 biology*, 15(4):e1006928, 2019.
- 604 [37] Sebastian Spreizer, Ad Aertsen, and Arvind Kumar. From space to time: Spatial inhomogeneities  
605 lead to the emergence of spatiotemporal sequences in spiking neuronal networks.  
606 *PLOS Computational Biology*, 15(10):e1007432, October 2019. doi: 10.1371/journal.pcbi.  
607 1007432. URL <https://doi.org/10.1371/journal.pcbi.1007432>.
- 608 [38] Carlo Michaelis, Andrew B. Lehr, and Christian Tetzlaff. Robust trajectory generation  
609 for robotic control on the neuromorphic research chip loihi. *Frontiers in Neurorobotics*,  
610 14, November 2020. doi: 10.3389/fnbot.2020.589532. URL [https://doi.org/10.3389/  
fnbot.2020.589532](https://doi.org/10.3389/<br/>611 fnbot.2020.589532).
- 612 [39] Amadeus Maes, Mauricio Barahona, and Claudia Clopath. Learning compositional se-  
613 quences with multiple time scales through a hierarchical network of spiking neurons.  
614 *bioRxiv*, 2020.
- 615 [40] Davide Spalla, Isabel Maria Cornacchia, and Alessandro Treves. Continuous attractors for  
616 dynamic memories. *eLife*, 10, September 2021. doi: 10.7554/elife.69499. URL [https://doi.org/10.7554/elife.69499](https://<br/>617 doi.org/10.7554/elife.69499).
- 618 [41] Andrew B Lehr, Arvind Kumar, and Christian Tetzlaff. Sparse clustered inhibition projects  
619 sequential activity onto unique neural subspaces. *bioRxiv*, pages 2023–09, 2023.
- 620 [42] Rodrigo Perin, Thomas K Berger, and Henry Markram. A synaptic organizing principle  
621 for cortical neuronal groups. *Proceedings of the National Academy of Sciences*, 108(13):  
622 5419–5424, 2011.
- 623 [43] X. Jiang, S. Shen, C. R. Cadwell, P. Berens, F. Sinz, A. S. Ecker, S. Patel, and A. S. Tolias.

- 624 Principles of connectivity among morphologically defined cell types in adult neocortex.  
625 *Science*, 350(6264):aac9462–aac9462, November 2015. doi: 10.1126/science.aac9462. URL  
626 <https://doi.org/10.1126/science.aac9462>.
- 627 [44] Xiangmin Xu, Nicholas D. Olivas, Taruna Ikrar, Tao Peng, Todd C. Holmes, Qing Nie, and  
628 Yulin Shi. Primary visual cortex shows laminar-specific and balanced circuit organization  
629 of excitatory and inhibitory synaptic connectivity. *The Journal of Physiology*, 594(7):1891–  
630 1910, March 2016. doi: 10.1113/jp271891. URL <https://doi.org/10.1113/jp271891>.
- 631 [45] Yangfan Peng, Federico J Barreda Tomas, Paul Pfeiffer, Moritz Drangmeister, Susanne  
632 Schreiber, Imre Vida, and Jörg RP Geiger. Spatially structured inhibition defined by po-  
633 larized parvalbumin interneuron axons promotes head direction tuning. *Science Advances*,  
634 7(25):eabg4693, 2021.
- 635 [46] Simon Weiler, Drago Guggiana Nilo, Tobias Bonhoeffer, Mark Hübener, Tobias Rose, and  
636 Volker Scheuss. Orientation and direction tuning align with dendritic morphology and  
637 spatial connectivity in mouse visual cortex. *Current Biology*, 32(8):1743–1753, 2022.
- 638 [47] Hemanth Mohan, Matthijs B. Verhoog, Keerthi K. Doreswamy, Guy Eyal, Romy Aardse,  
639 Brendan N. Lodder, Natalia A. Goriounova, Boateng Asamoah, A.B. Clementine B. Brak-  
640 spear, Colin Groot, Sophie van der Sluis, Guilherme Testa-Silva, Joshua Obermayer,  
641 Zimbo S.R.M. Boudewijns, Rajeevan T. Narayanan, Johannes C. Baayen, Idan Segev,  
642 Huibert D. Mansvelder, and Christiaan P.J. de Kock. Dendritic and axonal architec-  
643 ture of individual pyramidal neurons across layers of adult human neocortex. *Cere-  
644 bral Cortex*, 25(12):4839–4853, August 2015. doi: 10.1093/cercor/bhv188. URL <https://doi.org/10.1093/cercor/bhv188>.
- 645
- 646 [48] Rajeevan T Narayanan, Robert Egger, Andrew S Johnson, Huibert D Mansvelder, Bert  
647 Sakmann, Christiaan PJ De Kock, and Marcel Oberlaender. Beyond columnar organization:  
648 cell type-and target layer-specific principles of horizontal axon projection patterns in rat  
649 vibrissal cortex. *Cerebral cortex*, 25(11):4450–4468, 2015.
- 650 [49] L Federico Rossi, Kenneth D Harris, and Matteo Carandini. Spatial connectivity matches  
651 direction selectivity in visual cortex. *Nature*, 588(7839):648–652, 2020.
- 652 [50] Ye Li, Hui Lu, Pei lin Cheng, Shaoyu Ge, Huatai Xu, Song-Hai Shi, and Yang Dan.  
653 Clonally related visual cortical neurons show similar stimulus feature selectivity. *Nature*,  
654 486(7401):118–121, May 2012. doi: 10.1038/nature11110. URL <https://doi.org/10.1038/nature11110>.
- 655
- 656 [51] Zhiwen Ye, Matthew S Bull, Anna Li, Daniel Birman, Tanya L Daigle, Bosiljka Tasic,

- 657 Hongkui Zeng, and Nicholas A Steinmetz. Brain-wide topographic coordination of traveling  
658 spiral waves. *bioRxiv*, pages 2023–12, 2023.
- 659 [52] Walter J Freeman III. Waves, pulses, and the theory of neural masses. *Progress in theoretical*  
660 *biology*, 2(1):1–10, 1972.
- 661 [53] JR Wickens, R Kotter, and ME Alexander. Effects of local connectivity on striatal function:  
662 Simulation and analysis of a model. *Synapse*, 20(4):281–298, 1995.
- 663 [54] J Rinzel, D Terman, X-J Wang, and B Ermentrout. Propagating activity patterns in  
664 large-scale inhibitory neuronal networks. *Science*, 279(5355):1351–1355, 1998.
- 665 [55] G Bard Ermentrout and David Kleinfeld. Traveling electrical waves in cortex: insights  
666 from phase dynamics and speculation on a computational role. *Neuron*, 29(1):33–44, 2001.
- 667 [56] Alex Roxin, Nicolas Brunel, and David Hansel. Role of delays in shaping spatiotemporal  
668 dynamics of neuronal activity in large networks. *Physical review letters*, 94(23):238103,  
669 2005.
- 670 [57] Mikhail I Rabinovich, Pablo Varona, Allen I Selverston, and Henry DI Abarbanel. Dynamical  
671 principles in neuroscience. *Reviews of modern physics*, 78(4):1213, 2006.
- 672 [58] Doug Rubino, Kay A Robbins, and Nicholas G Hatsopoulos. Propagating waves mediate  
673 information transfer in the motor cortex. *Nature neuroscience*, 9(12):1549–1557, 2006.
- 674 [59] Jian-Young Wu, Xiaoying Huang, and Chuan Zhang. Propagating waves of activity in the  
675 neocortex: what they are, what they do. *The Neuroscientist*, 14(5):487–502, 2008.
- 676 [60] Evgueniy V Lubenov and Athanassios G Siapas. Hippocampal theta oscillations are trav-  
677 elling waves. *Nature*, 459(7246):534–539, 2009.
- 678 [61] James B Ackman, Timothy J Burbridge, and Michael C Crair. Retinal waves coordinate  
679 patterned activity throughout the developing visual system. *Nature*, 490(7419):219–225,  
680 2012.
- 681 [62] Jagdish Patel, Shigeyoshi Fujisawa, Antal Berényi, Sébastien Royer, and György Buzsáki.  
682 Traveling theta waves along the entire septotemporal axis of the hippocampus. *Neuron*, 75  
683 (3):410–417, 2012.
- 684 [63] Tatsuo K Sato, Ian Nauhaus, and Matteo Carandini. Traveling waves in visual cortex.  
685 *Neuron*, 75(2):218–229, 2012.
- 686 [64] Kazutaka Takahashi, Sanggyun Kim, Todd P Coleman, Kevin A Brown, Aaron J Suminski,

- 687 Matthew D Best, and Nicholas G Hatsopoulos. Large-scale spatiotemporal spike patterning  
688 consistent with wave propagation in motor cortex. *Nature communications*, 6(1):7169, 2015.
- 689 [65] Honghui Zhang and Joshua Jacobs. Traveling theta waves in the human hippocampus.  
690 *Journal of Neuroscience*, 35(36):12477–12487, 2015.
- 691 [66] Grégory Faye and Zachary P Kilpatrick. Threshold of front propagation in neural fields:  
692 An interface dynamics approach. *SIAM Journal on Applied Mathematics*, 78(5):2575–2596,  
693 2018.
- 694 [67] Randolph F Helfrich, Ian C Fiebelkorn, Sara M Szczepanski, Jack J Lin, Josef Parvizi,  
695 Robert T Knight, and Sabine Kastner. Neural mechanisms of sustained attention are  
696 rhythmic. *Neuron*, 99(4):854–865, 2018.
- 697 [68] Lyle Muller, Frédéric Chavane, John Reynolds, and Terrence J Sejnowski. Cortical trav-  
698 elling waves: mechanisms and computational principles. *Nature Reviews Neuroscience*, 19  
699 (5):255–268, 2018.
- 700 [69] Zachary W Davis, Lyle Muller, Julio Martinez-Trujillo, Terrence Sejnowski, and John H  
701 Reynolds. Spontaneous travelling cortical waves gate perception in behaving primates.  
702 *Nature*, 587(7834):432–436, 2020.
- 703 [70] Zachary W Davis, Gabriel B Benigno, Charlee Fletterman, Theo Desbordes, Christopher  
704 Steward, Terrence J Sejnowski, John H. Reynolds, and Lyle Muller. Spontaneous trav-  
705 eling waves naturally emerge from horizontal fiber time delays and travel through locally  
706 asynchronous-irregular states. *Nature Communications*, 12(1):6057, 2021.
- 707 [71] Sayak Bhattacharya, Scott L Brincat, Mikael Lundqvist, and Earl K Miller. Traveling  
708 waves in the prefrontal cortex during working memory. *PLoS computational biology*, 18(1):  
709 e1009827, 2022.
- 710 [72] Carlo R Laing, William C Troy, Boris Gutkin, and G Bard Ermentrout. Multiple bumps  
711 in a neuronal model of working memory. *SIAM Journal on Applied Mathematics*, 63(1):  
712 62–97, 2002.
- 713 [73] Sebastian Spreizer, Martin Angelhuber, Jyotika Bahuguna, Ad Aertsen, and Arvind Ku-  
714 mar. Activity dynamics and signal representation in a striatal network model with distance-  
715 dependent connectivity. *Eneuro*, 4(4), 2017.
- 716 [74] Sen Song, Per Jesper Sjöström, Markus Reigl, Sacha Nelson, and Dmitri B Chklovskii.  
717 Highly nonrandom features of synaptic connectivity in local cortical circuits. *PLoS Biology*,

- 718        3(3):e68, March 2005. doi: 10.1371/journal.pbio.0030068. URL <https://doi.org/10.1371/journal.pbio.0030068>.
- 720        [75] Sarah Rieubland, Arnd Roth, and Michael Häusser. Structured connectivity in cerebellar  
721        inhibitory networks. *Neuron*, 81(4):913–929, 2014.
- 722        [76] Claudia Espinoza, Segundo Jose Guzman, Xiaomin Zhang, and Peter Jonas. Parvalbumin+  
723        interneurons obey unique connectivity rules and establish a powerful lateral-inhibition mi-  
724        crocircuit in dentate gyrus. *Nature communications*, 9(1):4605, 2018.
- 725        [77] Segundo Jose Guzman, Alois Schlögl, Michael Frotscher, and Peter Jonas. Synaptic mech-  
726        anisms of pattern completion in the hippocampal ca3 network. *Science*, 353(6304):1117–  
727        1123, 2016.
- 728        [78] Nicolas Perez-Nieves, Vincent CH Leung, Pier Luigi Dragotti, and Dan FM Goodman.  
729        Neural heterogeneity promotes robust learning. *Nature communications*, 12(1):5791, 2021.
- 730        [79] Shira Sardi, Roni Vardi, Yael Tugendhaft, Anton Sheinin, Amir Goldental, and Ido Kanter.  
731        Long anisotropic absolute refractory periods with rapid rise times to reliable responsiveness.  
732        *Physical Review E*, 105(1):014401, 2022.
- 733        [80] Daniel Miner and Jochen Triesch. Plasticity-driven self-organization under topological con-  
734        straints accounts for non-random features of cortical synaptic wiring. *PLoS computational  
735        biology*, 12(2):e1004759, 2016.
- 736        [81] Kristen A Richardson, Steven J Schiff, and Bruce J Gluckman. Control of traveling waves  
737        in the mammalian cortex. *Physical review letters*, 94(2):028103, 2005.
- 738        [82] Leo Hiselius. spreizer-net. <https://github.com/leohiselius/spreizer-net>, 2021.
- 739        [83] Marcel Stimberg, Romain Brette, and Dan FM Goodman. Brian 2, an intuitive and efficient  
740        neural simulator. *Elife*, 8:e47314, 2019.
- 741        [84] Carlo Michaelis. Pelenet: a reservoir computing framework for loihi. *arXiv preprint  
742        arXiv:2011.12338*, 2020.
- 743        [85] Valentino Braitenberg and Almut Schuz. *Cortex: Statistics and Geometry of Neuronal  
744        Connectivity*. Springer Science and Business Media, Germany, 2013. ISBN 3662037335.
- 745        [86] Ken Perlin. An image synthesizer. *ACM Siggraph Computer Graphics*, 19(3):287–296,  
746        1985.
- 747        [87] Michael Avermann, Christian Tomm and Celine Mateo, Wulfram Gerstner, and Carl C. H.

- 748 Petersen. Microcircuits of excitatory and inhibitory neurons in layer 2/3 of mouse barrel  
749 cortex. *Journal of Neurophysiology*, Volume 107, Article 11, pp. 3116-3134, 2012.
- 750 [88] Sandrine Lefort, Christian Tomm, J.-C. Floyd Sarria, and Carl C.H.Petersen. The exci-  
751 tatory neuronal network of the c2 barrel column in mouse primary somatosensory cortex.  
752 *Neuron*, Volume 61, Issue 2, pp 301-316, 2009.
- 753 [89] Tomoki Fukai, Vladimir Klinshov, and Jun-Nosuke Teramae. Cortical networks with log-  
754 normal synaptic connectivity and their implications in neuronal avalanches. *Criticality in*  
755 *Neural Systems*, pp. 403 - 416, 2014.
- 756 [90] Carlo Michaelis. Think local, act global: robust and real-time movement encoding in  
757 spiking neural networks using neuromorphic hardware. 2022.
- 758 [91] Michael Berger, Naubahar Shahryar Agha, and Alexander Gail. Wireless recording from  
759 unrestrained monkeys reveals motor goal encoding beyond immediate reach in frontopari-  
760 etal cortex. *Elife*, 9:e51322, 2020.
- 761 [92] Wulfram Gerstner, Werner M. Kistler, Richard Naud, and Liam Paninski. *Neuronal Dy-*  
762 *namics: From Single Neurons to Networks and Models of Cognition*. Cambridge University  
763 Press, USA, 2014. ISBN 1107635195.

764

# Supplementary Figures

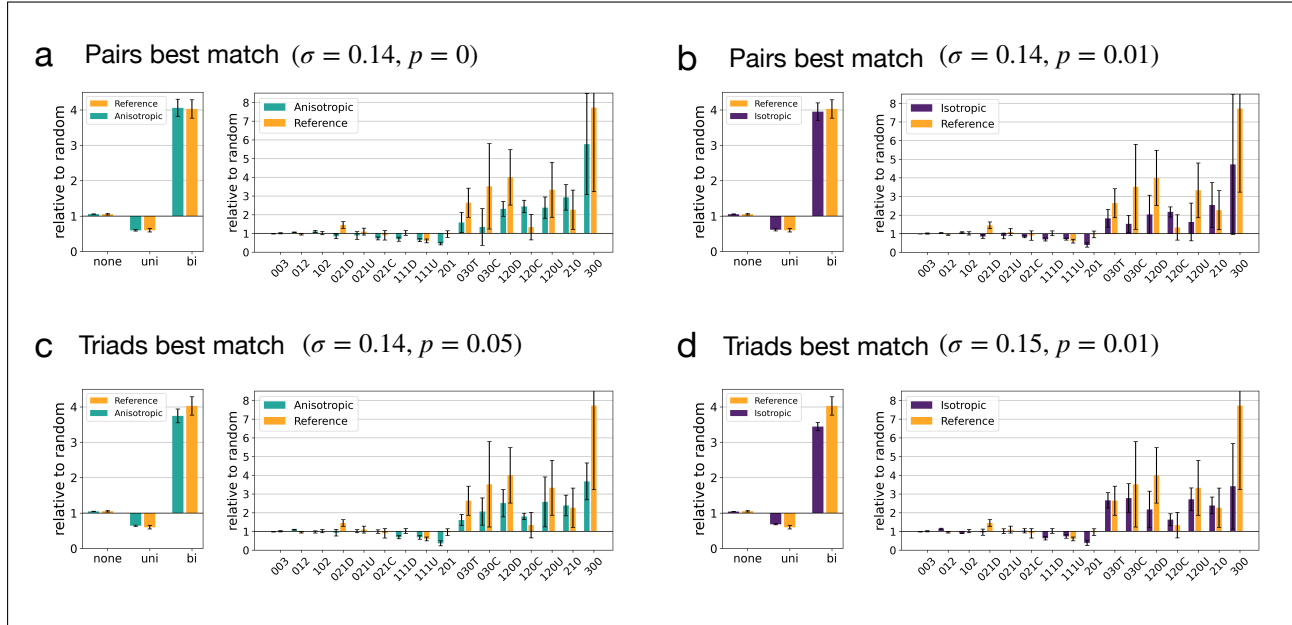


**Figure S1. Two and three neuron motif counts for parameters best matching experimental data<sup>74</sup> (related to Figs. 2 and 3).** (a) Two and three neuron motif distributions for the anisotropic network model for the parameters that minimized the mean relative error between the isotropic network vs. rat visual cortex data for motif counts in neuron pairs (see Fig. 2d). (b) Same as (a) but for the isotropic network (see Fig. 2c). (c) Two and three neuron motif distributions for the anisotropic network model for the parameters that minimized the mean relative error between the isotropic network vs. rat visual cortex data for motif counts in groups of three neurons (see Fig. 2c). (d) Same as (c) but for the isotropic network (see Fig. 3b).

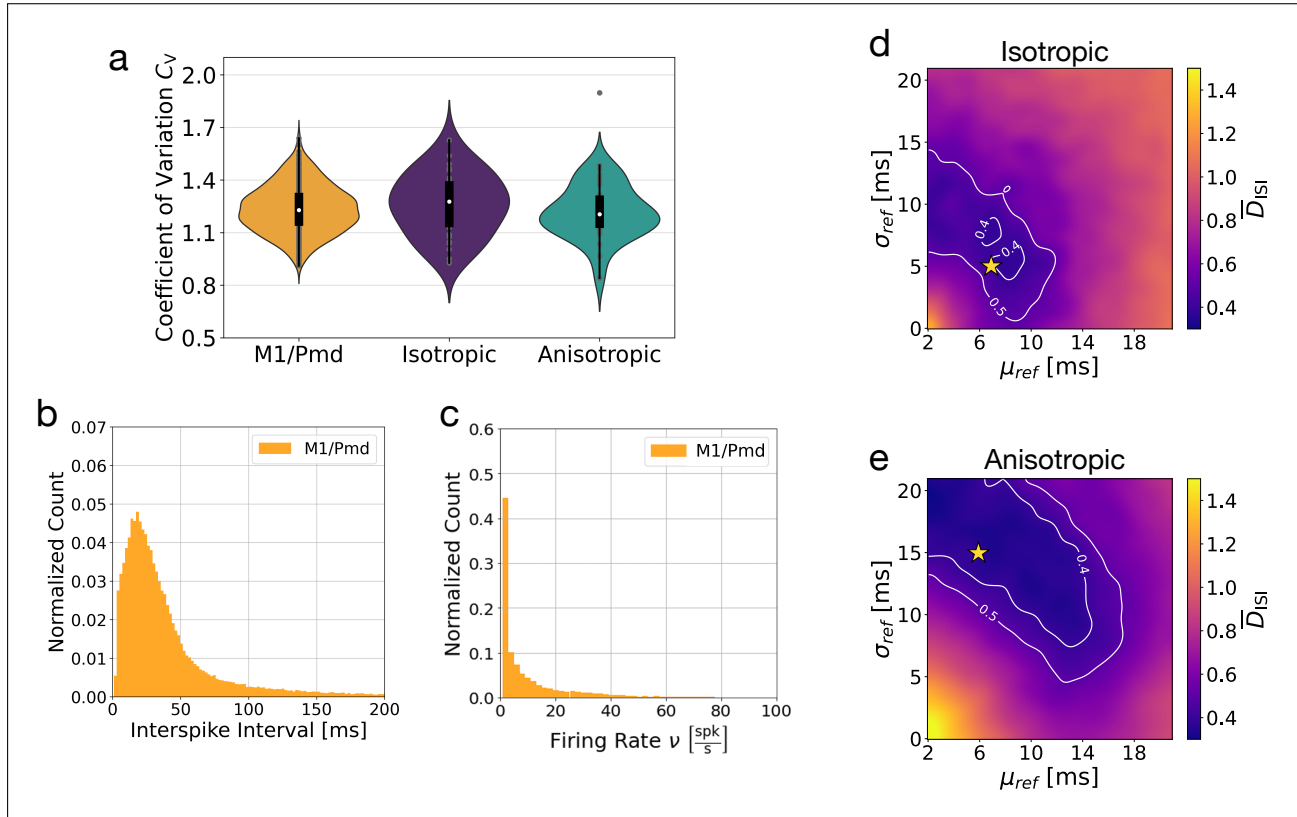


**Figure S2. Single neuron activity statistics match to second M1/PMd dataset (related to Fig. 4).** (a) Coefficient of variation for M1/PMd and the isotropic and anisotropic networks (reproduced from Fig. 4b). (b) ISI and firing rate distributions from the second monkey dataset. (d,e) Fits between data and models for isotropic and anisotropic connectivity.

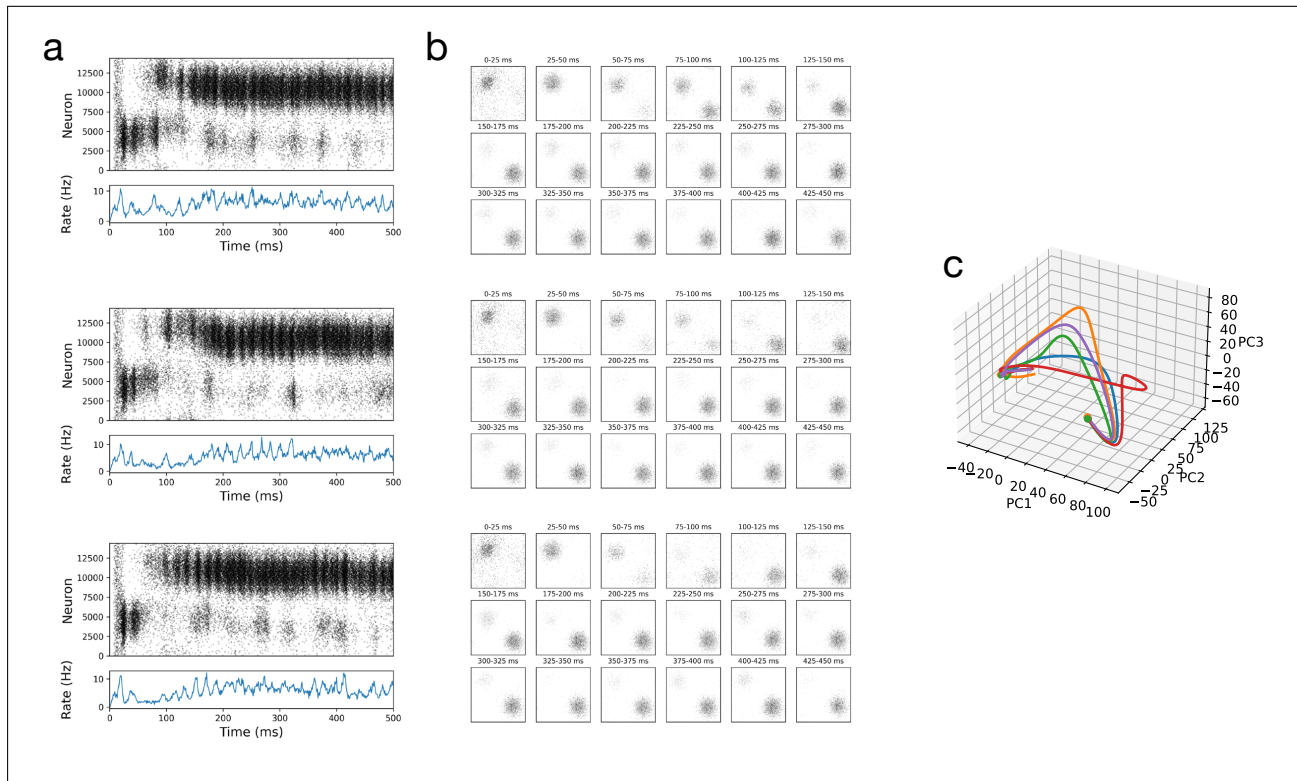


**Figure S3. Persistent spatially localized activity in network with symmetric distance-dependent connectivity fit to experimental data (related to Fig. 5).** (a) Spike rasters for three trials of one isotropic network simulation. (b) Activity over time organized in 2D according to neuron position shows bumps of activity. Bump persists at one location for a few hundred milliseconds. (c) Neural activity projected onto the first three principal components. Trajectories converge to one point in PC space and remain there, in agreement with the persistent bump of activity in the network.

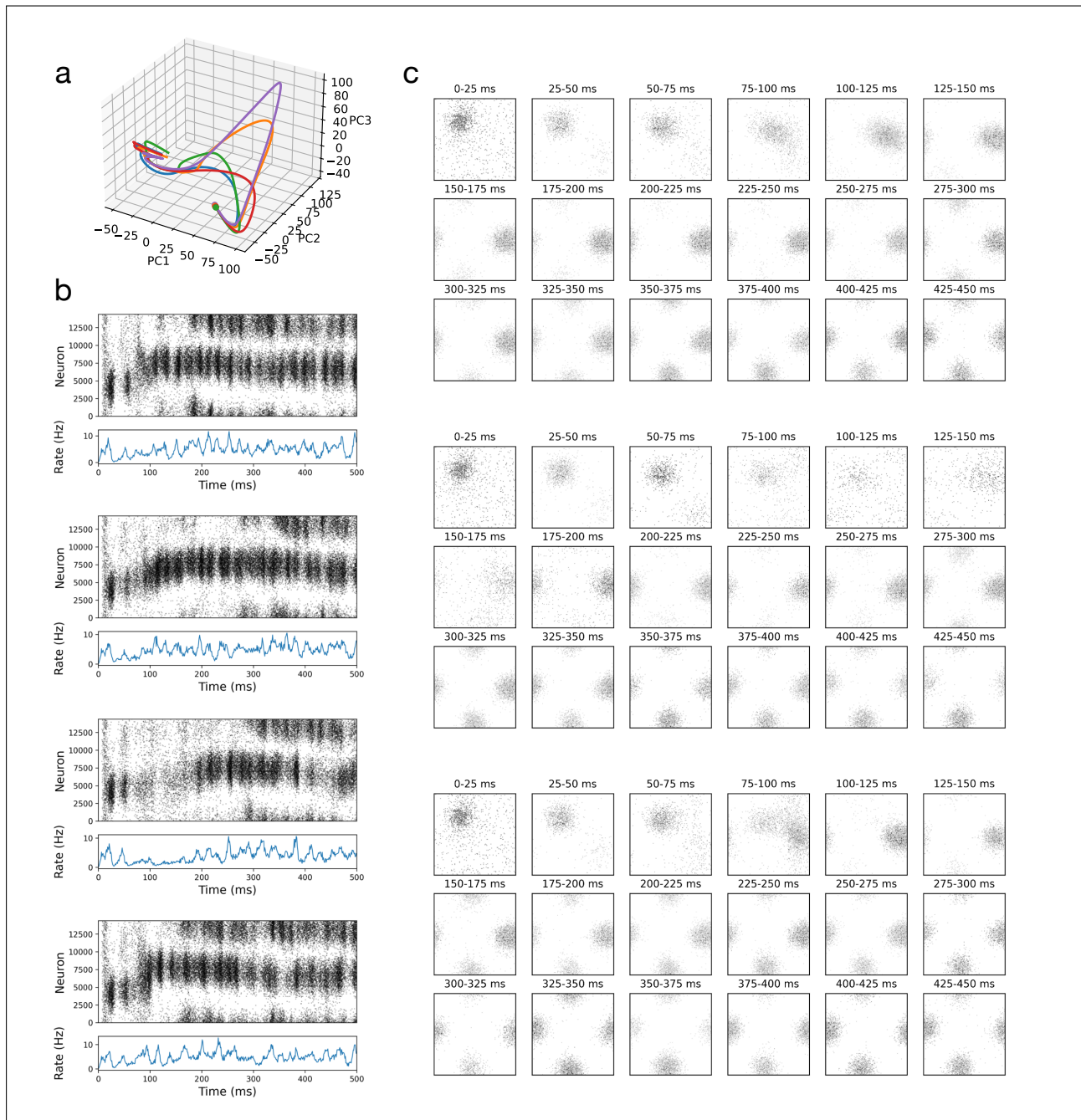


**Figure S4. Trajectories taking different paths in anisotropic network (related to Fig. 6).** (a) Neural activity projected onto the first three principal components. Trajectories for different trials take different paths related to the differences in spatiotemporal sequences (b) Spike rasters for four trials shows differences in activity in the early part of the trial before becoming similar thereafter. (c) Activity over time organized in 2D according to neuron position shows bumps of activity which are visibly different in the early part of the trial, becoming similar as the trial progresses.

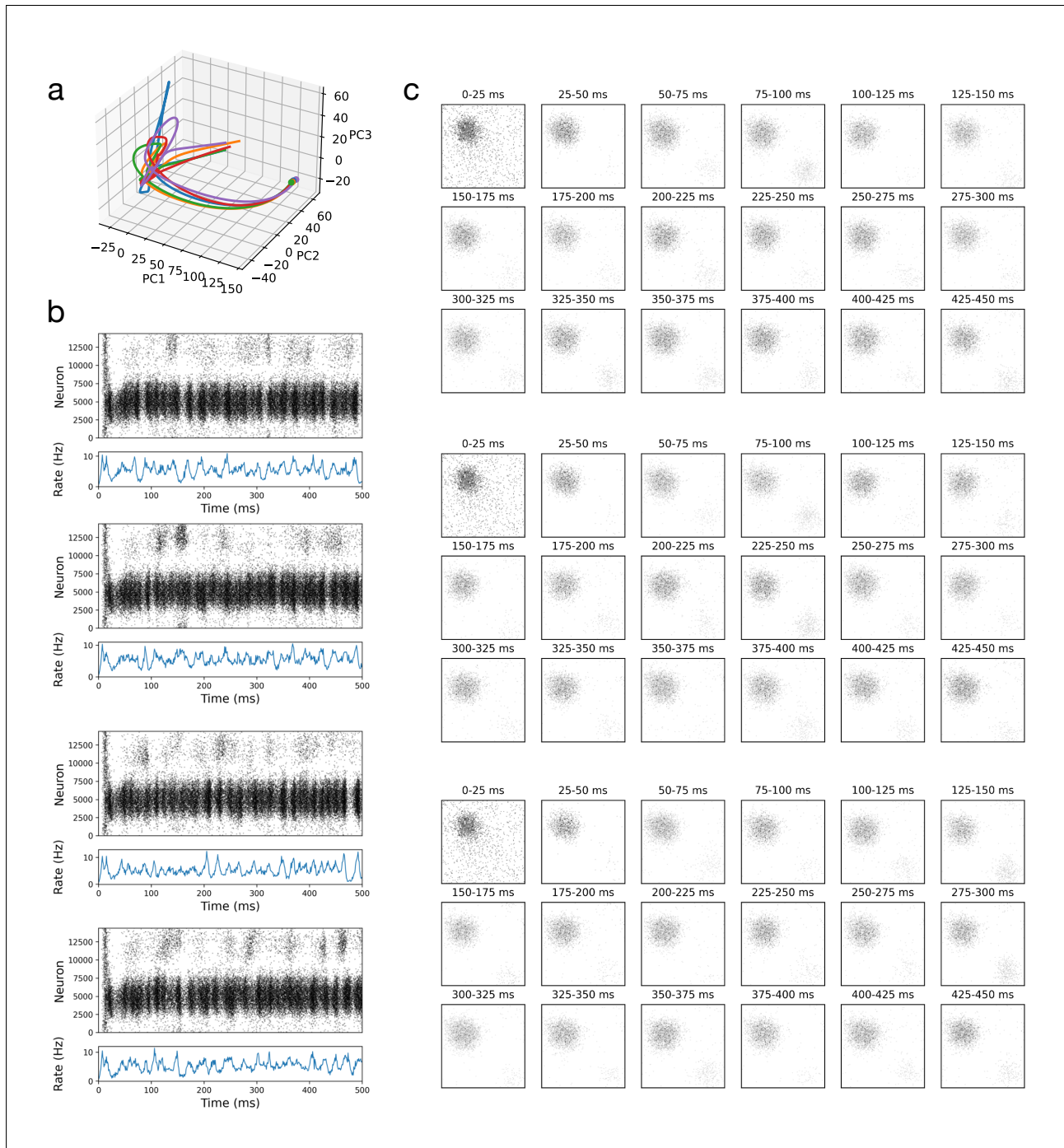


**Figure S5. Persistent spatially localized activity in anisotropic network with correlated asymmetric distance-dependent connectivity fit to experimental data (related to Fig. 6).** (a) Neural activity projected onto the first three principal components. Trajectory paths remain closely aligned and converge to one region in PC space in agreement with the persistent bump of activity in the network. (b) Spike rasters for four trials. (b) Activity over time organized in 2D according to neuron position shows bump persisting.